SPECTRAL ANALYSIS OF THINNING BEDS USING GROUND PENETRATING RADAR

A Thesis

by

RENEE ROSE FRANCESE

Submitted to the Office of Graduate Studies of
Texas A&M University
in partial fulfillment of the requirements for the degree of

MASTER OF SCIENCE

May 2012

Major Subject: Geophysics

SPECTRAL ANALYSIS OF THINNING BEDS USING GROUND PENETRATING RADAR

A Thesis

by

RENEE ROSE FRANCESE

Submitted to the Office of Graduate Studies of
Texas A&M University
in partial fulfillment of the requirements for the degree of

MASTER OF SCIENCE

Approved by:

Chair of Committee,	Mark Everett
Committee Members,	Rick Giardino
	Kevin McInnes
Head of Department,	Rick Giardino

May 2012

Major Subject: Geophysics

ABSTRACT

Spectral Analysis of Thinning Beds Using Ground Penetrating Radar. (May 2012)
Renee Rose Francese, B.S., Colorado School of Mines
Chair of Advisory Committee: Dr. Mark Everett

Ground Penetrating Radar (GPR) is a near surface geophysical method that has been used for applications including archaeological sites, groundwater contamination, and geological mapping. Though GPR has been used extensively, advancements on data processing had a great impact on data resolution. GPR is frequently used for shallow investigations because of the high resolution near the surface; however, it has limited depth of penetration and vertical bed resolution.

Vertical resolution is proportional to frequency. The thickness of beds in the subsurface is conventionally resolved to one-fourth the wavelength of the central frequency. The vertical resolution at a central frequency of 200 MHz in a beach environment is approximately 17 cm; however, that value does not accurately represent fine-scale lamina and pinching out of beds, which can be an order magnitude or more than the current resolution.

Complex trace analysis and spectral analysis have been used in seismic reflection for characterizing structures and stratigraphy. These "attributes" have been used to indicate hydrocarbon presence in industry. The same concept was applied to a theoretical GPR model and tested against actual data.

The theoretical GPR model was created to simulate a case in which two ideal 0° phase Ricker wavelets merge. The wavelets constructively "add" together to create a composite wavelet with double amplitude. Applying a spectral analysis reveals that an attribute in the form of instantaneous phase and instantaneous frequency can be used to image the beds merging.

The spectral analysis was applied to field data from North Padre Island National Seashore, Texas, to image "pinch-outs". Multiple survey arrays were collected using a 200 MHz frequency antenna to image internal dune structures. The results showed anomalous features at merging beds and contacts between interfaces. The results directly influence sedimentological and geomorphological interpretations of internal dune structure and can be used to better understand erosional processes in coastal sedimentary environments.

ACKNOWLEDGMENTS

There are many people who have been supportive of my efforts in completing this project. First, I would like to thank my fiance, family, and friends for their encouragement and love.

My project would not have been a success without Brad Weymer for his data and assistance. Brad was extremely helpful in giving a helping hand for data collection and allowing me to use his data for analysis. I would also like to thank Aileen Gaudinez, Mark Hickey and Scott Willson for this assistance in data collection.

Padre Island National Seashore was gracious enough to permit Texas A&M University to drive and collect data on the beach. They have been supportive of many students and have provided a great resource for more research.

I would also like to thank committee members Dr. Rick Giardino, Dr. Kevin McInnes, and Dr. Mark Everett for their support. Dr. Mark Everett has provided a great amount of insight and encouragement for the completion of the project.

Lastly, I would like to acknowledge the Department of Geology and Geophysics and the Berg Hughes Center for Petroleum and Sedimentary Systems for the ConocoPhillips Fellowship.

NOMENCLATURE

AGC	Automatic Gain Control
AVO	Amplitude Versus Offset
AVF	Amplitude Versus Frequency
CMP	Common Mid-Point
DFT	Discrete Fourier Transform
FT	Fourier Transform
GPR	Ground Penetating Radar
Rx	Receiver
TE	Transverse Electric
TM	Transverse Magnetic
Tx	Transmitter

TABLE OF CONTENTS

Page

Page

LIST OF TABLES

LIST OF FIGURES

FIGURE Page

FIGURE Page

FIGURE Page

FIGURE Page

1. INTRODUCTION

Ground penetrating radar (GPR) is a geophysical method in which a single short, transient pulse of electromagnetic radiation is used to penetrate the near-surface layers. GPR operates on similar principles to reflection seismology and sonar techniques, except that the subsurface is imaged based on a contrast of the electromagnetic, rather than acoustic, impedance at subsurface interfaces [Knight, 2001]. A typical GPR measurement is the amount of time it takes for electromagnetic waves to penetrate in the subsurface, reflect from impedance contrasts, and return to a receiver at the surface. GPR is an ideal method for applications in archaeology, groundwater investigation, geomorphology, construction science, environmental science, and geological mapping [Davis and Annan, 1989]. These applications were investigated by GPR as early as the 1980's and the number of GPR-related publications has since increased steadily [Neal, 2004].

The first use of electromagnetics to find buried objects was in 1904 [Neal, 2004]. Since then, GPR has grown to be a very popular method for contaminant plume mapping [Baker, 1998; Bradford, 1999], archaeological investigation [Gracia et al., 2000], rock glacier characterization [Berthling et al., 2001; Fukui et al., 2007], mapping of soil structures [Schmalz and Lennartz, 2002], detection of fractures [Deparis and Garambois, 2009], and characterization of sedimentary processes [Bailey and Bristow, 2000].

GPR is ideal for near surface imaging because of its high spatial resolution at shallow depths; however, one of the trade-offs of the method is its limited depth of penetration. The resolution limit of GPR, just as seismic reflection, is determined by the signal to noise ratio, and the frequency content and phase character of the source wavelet [Widess, 1973].

This thesis follows the style of Geophysics.

Vertical resolution is proportional to frequency, the higher the frequency, the better the vertical resolution [Neal, 2004]. The GPR wavelength λ is governed by velocity v and frequency f:

$$\lambda = \frac{v}{f}. \tag{1.1}$$

The classical limit of vertical resolution is $\lambda/4$ where λ is the central frequency, which is the most common frequency transmitted. In our case, the central frequency is 200 MHz, but the bandwidth is large and the source spectrum contains abundant low-frequency energy; in pulse radar, a short transmitted pulse implies a large bandwidth. To achieve a higher vertical resolution, the bandwidth must be increased because spatial resolution is determined by the transient pulse width, τ. A highly-localized function in the time domain corresponds to a broadband function in the frequency domain [Neal, 2004]. By the conventional seismic definition, a thin bed is an idealized as one whose thickness is less than $\lambda/8$ [Widess, 1973]. The resolution limits are discussed further in Section 2.6. If a bed is detected with thickness less than $\lambda/8$, the center of that bed lines up in time with the maximum negative amplitude of the reflected signal [Zeng, 2010]. The objective of this project is to image thin beds to a thickness of $\lambda/4$ or less using spectral analysis of GPR data.

1.1 Attribute Analysis

Attributes are characteristics of seismic reflection traces that reveal information about structures, stratigraphy and reservoir properties. Amplitude Versus Offset (AVO) and Amplitude Versus Frequency (AVF) are similar techniques that display useful seismic information, that cannot be discerned by directly examining the trace [Ikelle and Amundsen, 2005]. The offset is the distance between transmitter and receiver. A specific offset corresponds to a specific angle at which the waves reflect in the subsurface. Both are very useful in the petroleum industry because an anomalous AVO or AVF response may identify the possible presence of hydrocarbons. Typi-

cally, an AVF display consists of amplitude patterns in the offset-versus-frequency domain [Zeng, 2010]. The method of AVF has been successfully performed in seismic reflection studies by Zeng [2010]. He showed that a bed thins to a point where the reflections merge forming a "bright spot". Figure 1.1 shows the amplitude response of a thinning bed in which the upper and lower boundary reflections add constructively to create a much larger composite event.

Amplitude versus offset is widely accepted as a tool in industry and has become more commonly used in recent years. AVO displays amplitude with offset for common mid-point (CMP) data. The approach is similar to AVF but takes into consideration that the reflected energy varies with offset. An AVO display can reveal an anomalous zone of acoustic impedance as a result of hydrocarbon presence.

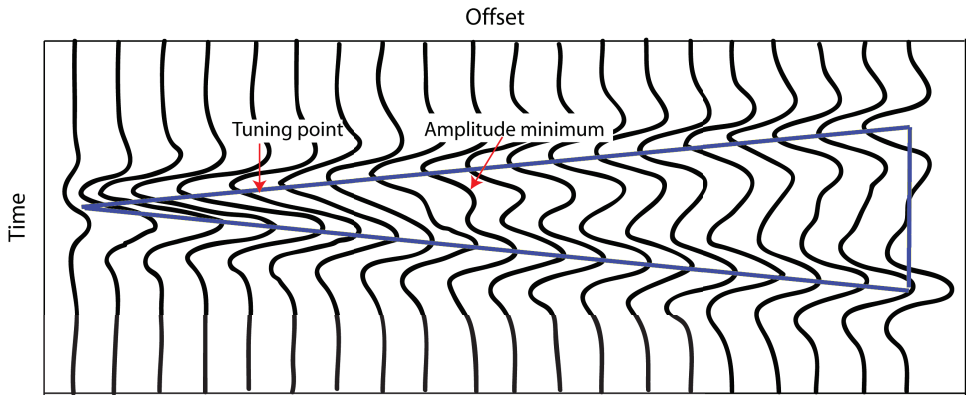

Fig. 1.1. Merging of reflections from the top and bottom of a thinning bed, shown here using synthetic seismic data. Modified from [Zeng, 2010].

The AVF and AVO responses are considered "attributes" of seismic data because they reveal otherwise elusive information on subsurface bodies as characterized by distinctive amplitude, shape, or arrival time of reflected waveforms [Ikelle and Amundsen, 2005]. In this study, GPR attributes will be analyzed to discern lateral variations in subsurface electromagnetic properties associated with thinning beds.

The fundamental basis for AVO analysis involves the Zoeppritz equations, which are a series of equations that describe reflection coefficients as a function of incident angle. The Zoeppritz equations incorporate subsurface velocities, impedance contrasts, and angles of the reflected and transmitted waves [Castagna and Backus, 1993]. Simplifications of these equations are given in Castanga [1993] as:

$$R_{pp}(\theta) \approx R_p + B \sin^2 \theta, \tag{1.2}$$

where B is termed the AVO gradient,

$$B \approx R_p - 2R_s, \tag{1.3}$$

θ is the angle of incidence, R_{pp} is the P-wave reflection coefficient at angle θ, R_p is the normal-incident P-wave reflection coefficient, and R_s is the normal-incident S-wave reflection coefficient. Though the physics of seismic and electromagnetic wave propagation are different, a similar methodology for GPR AVO analysis can be applied. Limited research has been done applying AVF and AVO to GPR data.

For the GPR-AVO application, a number of assumptions and simplifications were made by Bradford and Deeds [2006] to handle the complexities of the electromagnetic case. These assumptions include frequency-dependent material properties, radiation patterns that are the same for source and receiver, laterally homogeneous surface material, and transmission losses that do not vary significantly from place to place [Bradford and Deeds, 2006]. A GPR antenna behaves as a dipole and when placed on the ground, there is a radiated zone of energy [Annan and Jol, 2009]. The exact radiation patterns for a dipole antenna were originally derived in Engheta and Papas [1982] and simplified in Streich and van der Kruk [2007].

An amplitude correction to account for the GPR wave propagation characteristics was condensed by Bradford and Deeds [2006] into the expression:

$$\frac{A_x}{A_0} = \frac{P_x^2 G_0}{P_0^2 G_x} e^{-\alpha(r_x - r_0))} \frac{R_x}{R_0} \tag{1.4}$$

where $\frac{A_x}{A_0}$ is the corrected amplitude value, $\frac{P_x^2}{P_0^2}$ is the radiation pattern correction, $\frac{G_0}{G_x}$ is the geometric spreading correction, α is the attenuation term, and $\frac{R_x}{R_0}$ is the received signal. Subscripts x indicate the parameter value at offset x and subscript *0* is at near offset. After applying the corrections (Equation 1.4), the amplitude can be plotted against offset and interpreted.

Bradford and Deeds [2006] successfully identified thinning beds based on AVO analysis of common mid-point (CMP) GPR data. The data with corrected amplitudes were plotted against offset and compared with modeled data. The model and field data show trends of amplitude variation with offset.

The concepts of AVF analysis developed for seismic reflection are very similar when carried over tor GPR. The central idea is that an anomalous amplitude response is caused by an abrupt lateral variation of dielectric properties of the subsurface bed. This anomalous amplitude response shows an anomalous reading in the instantaneous frequency attribute. Research by Orlando [2002] showed that there were also anomalous attributes associated with subsurface contaminants. It is the goal of this project to use GPR attribute analysis for thinning beds in a coastal sedimentary system.

Such an attribute analysis was performed on GPR data collected at North Padre Island National Seashore, Texas. "Bright spots" are expected at locations where sedimentary beds pinch out at the lateral margins of washovers, for example. These may be indicators of recent storm deposits or other depositional environments found in coastal settings. Enhancing the vertical resolution can accurately portray thinning beds and in the near subsurface. Detection of bright spots associated with anomalous

attributes can be viewed as a method for enhancing vertical resolution beyond the classical $\lambda/4$ limit.

1.2 Motivation

The motivation for the project originates from a desire to analyze the lateral extent of sand sheets associated with sediment run-up from tsunamis in Thailand. The intent is to develop a method of identifying thinning beds in coastal sedimentary systems. The Texas Gulf of Mexico coastline is subjected to strong storm systems and contains washover and other deposits that are similar to sand sheets from tsunamis.

2. BACKGROUND

The theoretical foundation of GPR is based on electromagnetic wave propagation in heterogeneous media [Annan and Butler, 2005]. The most basic principles of GPR are provided herein; in-depth discussions may be found in Nabighian [1987] and Jackson [1999]. GPR wave propagation is characterized by attenuation, antenna radiation patterns and geometric spreading.

2.1 Electromagnetic Theory

Maxwell's equations, which are reviewed in Annan and Butler [2005], describe the relationship between electrical and magnetic fields.

A constitutive equation describes how subsurface charge carriers respond to the application of an electric field. Specifically, charge transport is governed by Ohm's law:

$$\vec{J} = \sigma \vec{E} \tag{2.1}$$

where $\vec{E}$ is the electric field [V/m], σ is electrical conductivity [S/m], and $\vec{J}$ is the current density [A/m^2] [Olhoeft, 1998]. Charge storage is governed by a second constitutive equation:

$$\vec{D} = \epsilon \vec{E} \tag{2.2}$$

where ϵ is the dielectric permittivity [F/m] and $\vec{D}$ is the electric flux density [C/m^2] [Olhoeft, 1998]. Magnetic permeability describes how an elementary loop of electric current, known as a magnetic dipole, responds to a magnetic field:

$$\vec{B} = \mu \vec{H} \tag{2.3}$$

where $\vec{H}$ is the magnetic field [A/m], $\vec{B}$ is the magnetic flux density [T], and μ is the magnetic permeability [H/m] [Olhoeft, 1998]. The quantities σ, ϵ, and μ are the elec-

tromagnetic material properties where ϵ_0=8.85x10^{-12}(F/m) and μ_0=4πx10^{-7}(H/m) [Annan and Butler, 2005]. Dielectric permittivity varies if the medium contains polar molecules, such as water, and μ varies if the medium contains permanent magnetization, such as in the presence of iron mineralization.

Table 2.1
Dielectric constants (ϵ), electrical conductivity (σ), velocity (v), and attenuation (α) observed in geologic materials at 10-100MHz frequency [Davis and Annan, 1989].

Material	ϵ	σ(mS/m)	v (m/ns)	α (dB/m)
Air	1	0	0.30	0
Distilled water	80	0.01	0.033	2x10^{-3}
Fresh water	80	0.5	0.033	0.1
Sea water	80	3x10^4	0.01	10^3
Dry sand	3-5	0.01	0.15	0.01
Saturated sand	20-30	0.1-1.0	0.06	0.03-.3
Limestone	4-8	0.5-2	0.12	0.4-1
Shales	5-15	1-100	0.09	1-100
Silts	5-30	1-100	0.7	1-100
Clays	5-40	2-1000	0.06	1-300
Granite	4-6	0.01-1	0.13	0.01-1
Dry Salt	5-6	0.01-1	0.13	0.01-1
Ice	3-4	0.01	0.16	0.01

Table 2.1 represents typical values for dielectric constants (ϵ), electrical conductivity (σ), electromagnetic wave velocity (v), and attenuation (α) observed in geologic materials at 10-100 MHz frequency. Velocities in the table were calculated using equation 2.4.

2.2 Electromagnetic Wave Properties

The wavefront or raypath resulting from energy radiated by an electromagnetic source spreads radially. Rays are perpendicular to wavefronts, as seen in Figure 2.1. Properties of electromagnetic waves include phase velocity, attenuation, and electromagnetic impedance [Annan and Butler, 2005]. Electromagnetic fields propagate over a wide range of frequencies. GPR applications typically use a frequency range between 1 MHz and 1 GHz. Within this frequency range, in lossless near-surface media, electromagnetic wave propagation is controlled by spatial variations of dielectric permittivity in lossless media [Annan and Butler, 2005]. At the maximum frequency of this range, the velocity becomes independent of frequency and conductivity; this is called the "GPR plateau" (Figure 2.2). In low-loss Earth materials,

$$v = \frac{c}{(\epsilon')^{1/2}} \tag{2.4}$$

where c is the speed of light (c=3x10^8 m/s), ϵ' is the relative permittivity or dielectric constant, and v is velocity (m/ns) [Davis and Annan, 1989].

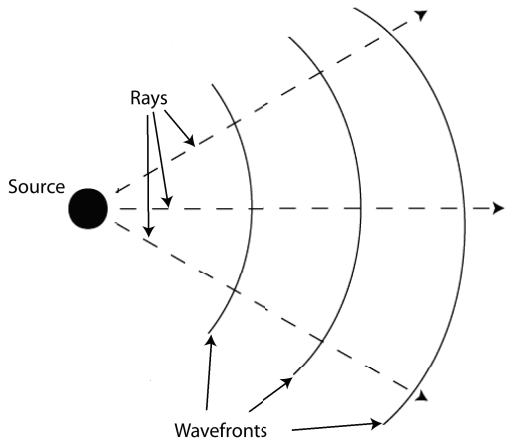

Fig. 2.1. Wavefronts are surfaces of equal phase for waves traveling radially outward from a source. Modified from Annan and Butler [2005].

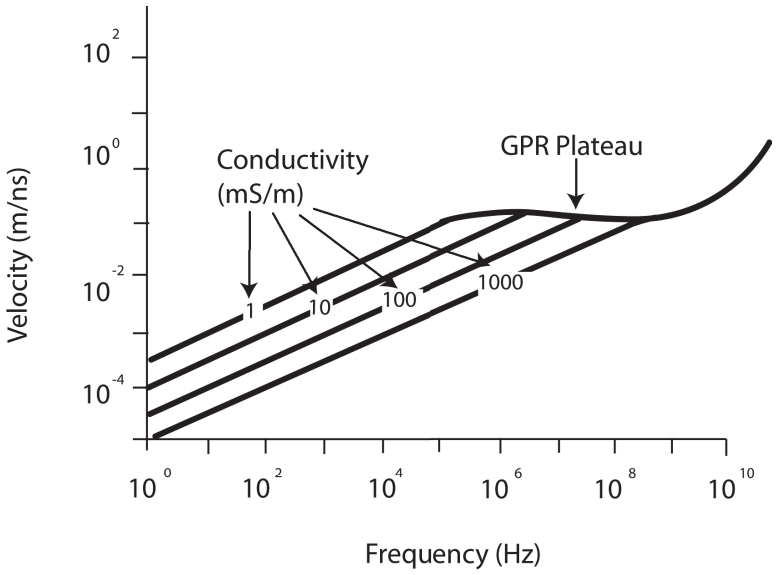

Fig. 2.2. Plot of relationship between velocity and frequency for varying conductivities. The velocity becomes independent of frequency in the "GPR plateau". Modified from Davis and Annan [1989].

The success of GPR replies heavily on the occurrence of impedance contrasts within the ground [Reynolds, 1997]. The most important ray paths between transmitter and receiver are those associated with the air wave, ground wave, refracted waves, and transmitted waves (Figure 2.3). Most of the electromagnetic energy is directed into the subsurface, although some is lost in the air. The air wave travels at the speed of light and is the first wave to be recorded. The second fastest is the ground wave which results from the propagation of the transmitted energy to the receiver without encountering any obstruction. This is especially apparent when the antennas are not shielded [Neal, 2004]. The strong signal from the air wave and ground wave may mask reflectors close to the surface. A lateral wave results from shallow reflections that approach the surface at the critical angle (θ_c) and are refracted along the air-ground interface [Neal, 2004]. Some of the electromagnetic energy from the transmitter also reflects from a subsurface reflector and travels back

to the reflector as a reflected signal. The amplitude reflection coefficient is expressed as:

$$R = \frac{\sqrt{\epsilon_2} - \sqrt{\epsilon_1}}{\sqrt{\epsilon_2} + \sqrt{\epsilon_1}} \tag{2.5}$$

where ϵ_1 and ϵ_2 are dielectric constants of a two layer system. Typically, the dielectric constant (ϵ) increases with depth and is almost entirely dependent on the subsurface water content, which increases with depth into the vadose zone [Reynolds, 1997].

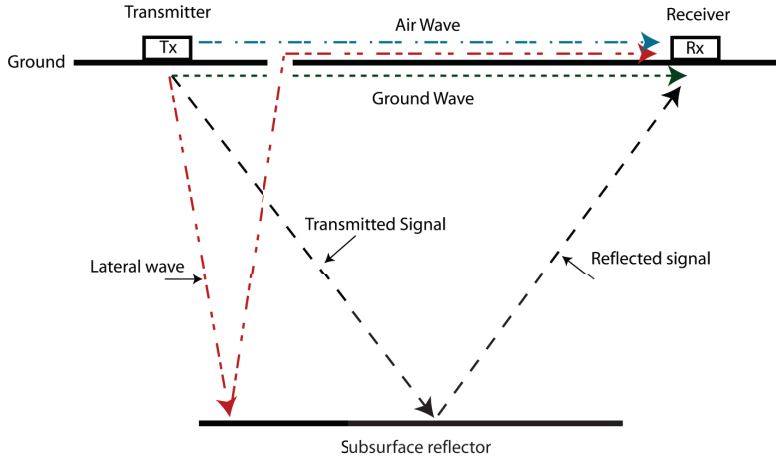

Fig. 2.3. Diagram of reflected waves between the ground and subsurface reflector. Modified from Neal [2004]

2.3 Operation

A GPR system is comprised of a transmitting and a receiving antenna, a signal generator, and a receiver that records the output. The radar system transmits a signal that propagates through the subsurface to the receiving antenna. The travel time for the radar wave to be transmitted and received is on the order of several thousand ns [Reynolds, 1997]. The transmitter generates a pulse of radio waves at a frequency governed by the length of the antennas. The short transient pulse generates a broadband signal centered on the fundamental frequency of an antenna of length L. Once data are collected, they are displayed as a scan of the amplitude

at each transmitter receiver offset as a function of two-way travel time [Reynolds, 1997]. A simplified diagram of the radar system and display can be seen in Figure 2.4.

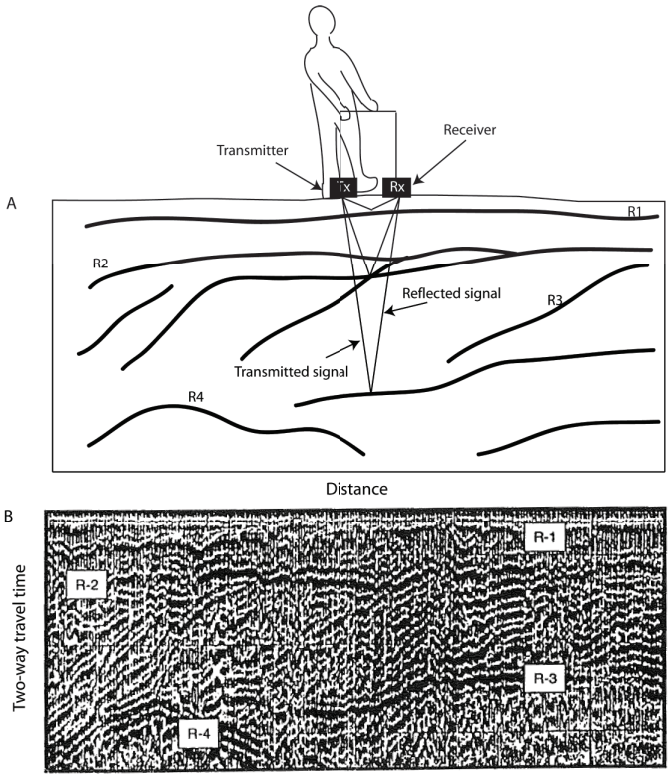

Fig. 2.4. The user moves the transmitter and receiver along the surface at a specific array spacing. In our case, the initial separation of the transmitter and receiver is 1 m and then the device is moved over 0.25 m. The diagram shows a radargram of amplitudes (B) resulting from a GPR survey and the interpreted subsurface section (A). Modified from Reynolds [1997].

There are several possible orientations of antenna pairs including transverse electric (TE) and transverse magnetic (TM). The various combinations of the transmitter (Tx) and receiver (Rx) pair configurations are shown in Figure 2.5.

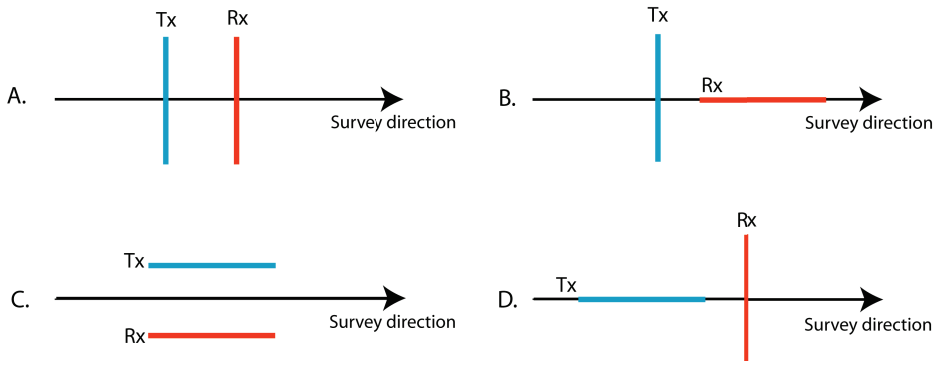

Fig. 2.5. Antenna orientation with respect to survey direction. A. TE mode parallel component, B. TE mode cross component, C. TM mode parallel component, D. TM mode cross component. Modified from Lutz et al. [2003]

The orientation of the antennas can greatly affect how subsurface reflectors are imaged. The TE mode is the typical operating mode because it is optimal for imaging when the profile direction is oriented perpendicular to a linear subsurface feature (e.g. a long metal pipe). The TE mode is not affected by depolarization due to reflections from a planar interface. The TM mode is most useful for geological imaging when the profile direction is oriented perpendicular to a subsurface feature (e.g. a fault) [Lutz et al., 2003]. There are important considerations concerning the orientations of the antennas. Radiation patterns describe the local orientation of the $\vec{E}$ field radiated by the antenna (see Section 2.4.2). Ideally, data should be collected using different orientations, known as "polarimetric GPR", to account for polarization and depolarization effects.

2.4 GPR limitations

There are inherent limitations associated with GPR as far as accurate subsurface imaging is concerned. The limitations are a result of how electromagnetic energy is produced and the manner by which radar waves propagating in the heterogeneous subsurface can interact with subsurface targets.

2.4.1 *Attenuation*

Attenuation can be extremely high but is variable under different environmental conditions [Annan and Jol, 2009]. A low-attenuation environment would allow depth of penetration up to 10 m whereas a high-attenuation environment may restrict penetration depths to less than 1 m [Annan and Jol, 2009]. Attenuation α is expressed as:

$$\alpha = \frac{1}{2}\sigma\sqrt{\frac{\mu}{\epsilon}}, \tag{2.6}$$

where σ is electrical conductivity [S/m], ϵ is the dielectric permittivity [F/m], and μ is the magnetic permeability [H/m] [Annan and Butler, 2005]. Attenuation in natural materials is caused by ohmic loss and scattering [Annan and Jol, 2009]. The combination of the attenuation mechanism is increased at higher frequencies, decreasing the signal penetration into the subsurface. Figure 2.6 shows that for an equal reflectivity earth containing four reflectors, the high-loss case exhibits greater attenuation compared to the low-loss case.

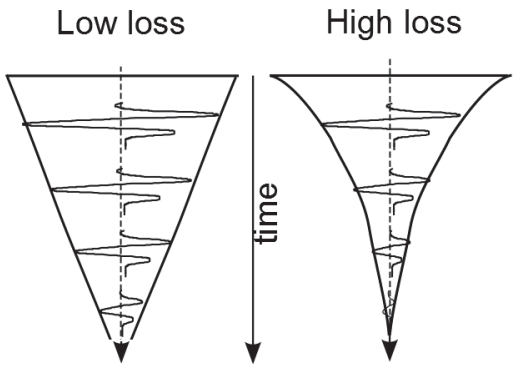

Fig. 2.6. Low loss of depth of penetration at lower frequencies (left) and high loss of depth of penetration at higher frequencies (right). Modified from Annan and Jol [2009].

The amplitude of the wavelets decreases with time and this decrease is more pronounced in the high-loss case [Annan and Jol, 2009]. In order to account for the attenuation at depth, automatic gain control (AGC) can be applied to the data (see Section 4.4).

2.4.2 *Radiation Patterns*

A standard GPR antenna is a straight wire segment, or dipole, that when placed on the ground surface and energized, radiates an electromagnetic field [Annan and Jol, 2009]. The radiation pattern is a combination of transverse electric (TE) mode and transverse magnetic (TM) modes. The two radiation patterns corresponding to TE and TM modes are side-by-side in Figure 2.7. The top hemisphere contains the air wave radiation pattern above the ground. The bottom hemisphere contains the radiation pattern in the subsurface. Figure 2.8 compares the radiation patterns for various dielectric constants. The peaks in the TE mode pattern occur at the critical angle (θ_c) of the air-ground interface Annan and Jol [2009]. The critical angle is represented as:

$$\theta_c = sin^{-1}\frac{1}{\sqrt{\epsilon}}. \tag{2.7}$$

The shape of the radiation pattern changes as the ground properties change. Figure 2.8 illustrates a sequence of radiation patterns for the TE mode as the ground dielectric constant varies from 3.2 (∼dry, consolidated material) to 80 (∼water). Computations of approximate far-field radiation patterns are found in Streich and van der Kruk [2007]. The radiation patterns are 3-dimensional and describe the radiated field in all directions from the source. Though some energy is lost in the air, most of the energy is radiated downward, depending on ϵ.

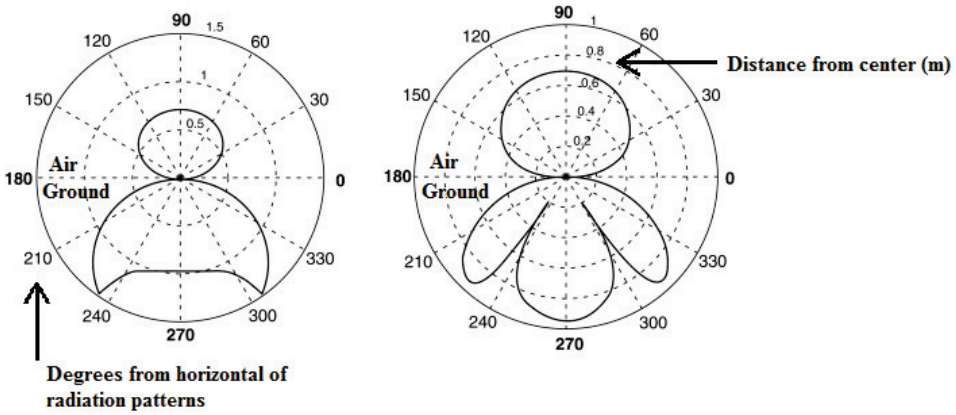

Fig. 2.7. Plan view of radiation patterns for TE mode (left) and TM mode (right) for a 3.2 dielectric constant. Modified from Annan and Jol [2009].

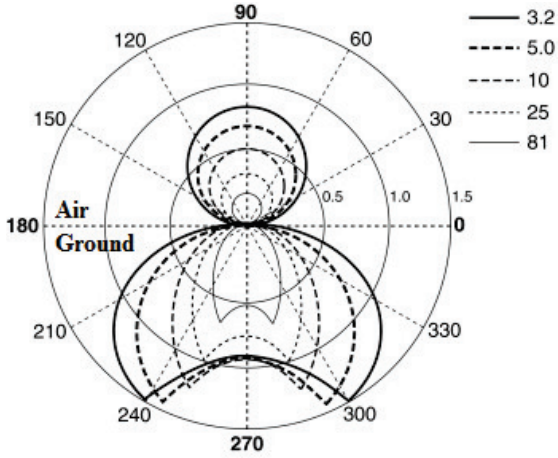

Fig. 2.8. Plan view of radiation patterns for TE mode for varying dielectric constants [Annan and Jol, 2009].

2.4.3 *Geometric Spreading*

The two components of geometric spreading are vertical and lateral spreading. Lateral spreading is calculated by using the Fresnel equations [Bradford, 1999]. The Fresnel equations assume that the polarization of the incident wave is parallel to the

plane of incidence for electrodynamics. The reflected electric field is $\tilde{E_{0_R}}$, $\tilde{E_{0_T}}$ is the transmitted electric field, $\tilde{E_{0_I}}$ is the obliquely incident electric field, θ_T is the angle of transmission, θ_I is the angle of incidence, μ_1 and μ_2 are the magnetic permeability of medium 1 and 2, and n_1 and n_2 are the index of refraction for medium 1 and 2 [Griffiths, 1989].

$$\tilde{E_{0_R}} = \left(\frac{\alpha-\beta}{\alpha+\beta}\right)\tilde{E_{0_I}}, \tag{2.8}$$

$$\tilde{E_{0_T}} = \left(\frac{2}{\alpha+\beta}\right)\tilde{E_{0_I}}, \tag{2.9}$$

where

$$\alpha \equiv \frac{cos\theta_T}{cos\theta_I},$$
$$\beta \equiv \frac{\mu_1 n_2}{\mu_2 n_1}.$$

The set of equations (2.8 and 2.9) are derived under the assumption of a monochromatic electromagnetic plane wave incident on a half-space boundary separated by two isotropic media [Bradford and Deeds, 2006]. This may not always be a good approximation for real-world scenarios.

The Fresnel zone decomposes the geometric spreading waveform into a number of sinusoidal signals and can be regarded as the zone of diffraction from a circular aperture [Annan and Jol, 2009]. From this, lateral resolution ($\triangle$l) can be expressed as:

$$\triangle l = \sqrt{\frac{d\lambda_c}{2}} \tag{2.10}$$

where λ_c is the central frequency wavelength and d is the vertical distance from the surface to the target [Annan and Jol, 2009].

Vertical resolution is defined as the ability to resolve two closely spaced features [Knapp, 1990]. The classical limit of resolution is $\lambda/4$. By the conventional seismic definition, a thin bed is one whose thickness is less than $\lambda/8$ [Widess, 1973]. The

enhancement of vertical resolution of thin beds is through GPR attribute analysis, which is the main focus of this research project.

2.5 Fourier Transforms

In order to analyze the Amplitude Versus Frequency characteristics of a trace, a discrete Fourier transform (DFT) is applied. A Fourier transform (FT) is a conversion of a function of time into a function of frequency [Oppenheim and Schafer, 2010]. The continuous transform is defined by:

$$F(\omega) = \int_{-\infty}^{\infty} f(t) exp(-2\pi i \omega t) dt \tag{2.11}$$

where *F(ω)* is the Fourier transform, t is the time, and ω is the frequency [Oppenheim and Schafer, 2010]. The Fourier transform decomposes a waveform *f(t)* into a number of sinusoids each having a complex amplitude *F(ω)*. When the time function *f(t)* is discretized, a discrete Fourier transform is needed. The DFT and its inverse are defined by:

$$X_k = \sum_{j=0}^{N-1} x_j exp(-2\pi i j k/N), \tag{2.12}$$

$$x_j = \frac{1}{N} \sum_{k=0}^{N-1} X_k exp(2\pi i j k/N), \tag{2.13}$$

where X_k and x_j are assumed to be periodic sequences, and N is is the number of time samples [Oppenheim and Schafer, 2010]. Equation 2.12 is the discrete Fourier transform (DFT) and Equation 2.13 is the inverse discrete Fourier transform (IDFT). The equations are similar, differing only in a constant multiplier and the sign of the exponents. A DFT will be applied to common offset traces to analyze their amplitude and phase spectra. The results may show a characteristic change in the

phase indicative of a chance in traces reflected by a thinning bed. The trace-to-trace changes in phase spectrum can be tracked using GPR scans over a thinning bed.

Observing pinch-outs by trace-to-trace amplitude analysis was performed using synthetic seismic reflection data in a paper by Zeng [2009]. When looking at the seismic traces, where the beds pinched out, the amplitude becomes very large and is visually seen as a "bright spot" (Figure 1.1).

In order to show the trace-to-trace variation in the phase spectra, a DFT of GPR common offset traces was performed. The steps taken for the spectral analysis were performed based on the tutorial on complex seismic trace analysis by Barnes [2007]. There are two components in a Fourier transform, the amplitude and the phase:

$$|F(\omega)| = \sqrt{a^2 + b^2}, \tag{2.14}$$

$$\Phi(\omega) = tan^{-1}\left(\frac{b}{a}\right), \tag{2.15}$$

derived from b, the imaginary part, and a, the real part of the complex function F(ω). Equation 2.14 is the absolute value of the two components and results in an amplitude value.

The phase information is then used to calculate the instantaneous frequency (ω) [Taner et al., 1979]:

$$\omega(t) = \frac{d\Phi(t)}{dt}. \tag{2.16}$$

Trace-to-trace variations in phase and instantaneous frequency are termed attributes of the GPR data. Matlab code to compute GPR attributes is given in Appendix 1

2.6 Resolution Limit

There has long been great interest in the of resolution limit of seismic data. Discussions on thin bed resolution limits appear in Widess [1973] "How thin is a

thin bed?" and Ricker [1953] "Wavelet Contraction, Wavelet Expansion, and the Control of Seismic Resolution." Over time, methods for resolving thin beds have improved. There are two criteria that have been used in thin bed resolution: the Widess and Ricker Criterion and the Rayleigh Criterion.

The resolution for GPR is one quarter of the dominant wavelength, seen in equation 1.1. Therefore, at a frequency of 200 MHz and estimated velocity of .14 m/ns the vertical resolution limit is:

$$\begin{aligned} \lambda &= \frac{.14\text{m/ns}}{200\text{MHz}} \\ \lambda &= .7\text{m} \\ \lambda/4 &= 17.5\text{cm} \end{aligned}$$

This means that two features in the subsurface can be detected only if they are separated by more than 17.5 cm. In sedimentary depositional systems, this most certainly is not the case where a thinning beds can have variable thicknesses of less than 1 mm to 10 mm in some cases [Neal, 2004].

2.6.1 *Rayleigh's Criterion*

The Rayleigh criterion was first used for optical reflections in which the classical resolution limit is $\lambda/4$ [Jenkins and White, 1957]. Rayleigh's criterion is the point at which the apparent bed thickness is the same as its true thickness. This is calculated by setting the derivative of the probing wavelet to zero [Kallweit and Wood, 1982]. Rayleigh's criterion is applicable to the case where a wavelet interacts with two interfaces of the same polarity [Zeng, 2009]. Rayleigh's criterion suggests that the thin bed is unresolved when the peak-to-trough separation is less than one-half of the bed thickness [Kallweit and Wood, 1982].

2.6.2 *Widess and Ricker Criteria*

Widess and Ricker have developed similar criteria for describing the resolution of thinning beds but they rely on synthetic responses of models in which two closely-spaced beds are isolated from other acoustic impedance contrasts [Knapp, 1990]. Ricker's criterion considers the superposition of two identical waveforms as a function of their separation. The limit of resolvability occurs at bed separation for which the composite waveform has a curvature of zero, or a flat spot, at its central maximum [Ricker, 1953]. Widess' criterion also studied a composite waveform constructed by convolving a zero-phase wavelet with two reflectivity spikes of equal amplitude and opposite polarity [Widess, 1973]. Both criteria use the basic model of a wedge with reflections from its top and bottom. A detailed description of the similarities and differences of the two criteria is presented in Kallweit and Wood [1982].

Figure 2.9 illustrates a phase shift between two wavelets when displaced slightly due to reflection from the top and bottom of a thin bed. The displaced time between wavelets dependsl to velocity and bed thickness:

$$\triangle T = \frac{2b}{v_b} \tag{2.17}$$

where $\triangle$T is displaced time, v_b is the velocity of the bed and b is the thickness of the bed [Widess, 1973]. The velocity of the bed is then used to estimate the wavelength (λ_b, expressed in terms of wavelengths):

$$\lambda_b = \tau v_b \tag{2.18}$$

where τ is the predominant period of the wavelet [Widess, 1973].

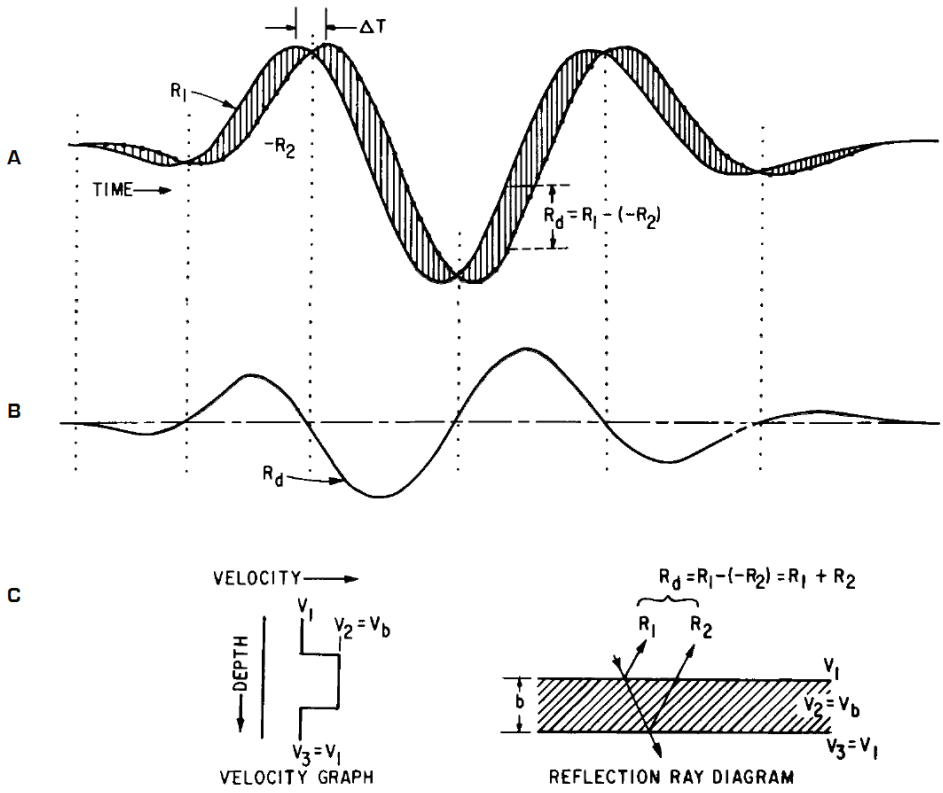

Fig. 2.9. Identical wavelets shifted slightly due to the reflection of a thin bed [Widess, 1973].

This relationship was determined using synthetic seismic traces when $\tau = 0.5$ s. The traces exhibited interference between reflections from the top and bottom surfaces of the bed, as a function of bed thickness. When the bed thickness becomes less than $\lambda/8$, the character of the reflection is the time derivative of the incident wavelet [Ricker, 1953]. Widess [1973] determined an inverse relation between bed thickness to wavelength:

$$A_d \cong 4\pi Ab/\lambda_b \tag{2.19}$$

where A_d is the maximum amplitude of the wavelet, A is the mean amplitude of the predominant peak and trough, b is bed thickness, and λ_b is the wavelength [Widess, 1973]. This relationship is valid under the assumption that the two media bounding

the thin bed have the same acoustic impedance [Widess, 1973]. The Widess and Ricker criteria are based on closely spaced reflectors of equal polarity and strength [Ricker, 1953].

Zeng [2009] determined that the work done by Widess [1973] and Ricker [1953] is valid for certain theoretical applications; however, a more practical resolution limit for thin beds is $\lambda/4$ using the Rayleigh criterion that was first established by Jenkins and White [1957].

2.6.3 *Ricker Wavelet with 0° and 90° Phase*

Figure 2.10 illustrates the difference between resolution using the Ricker criterion and the Rayleigh criterion for 90° and 0° wavelets (Model 1-3).

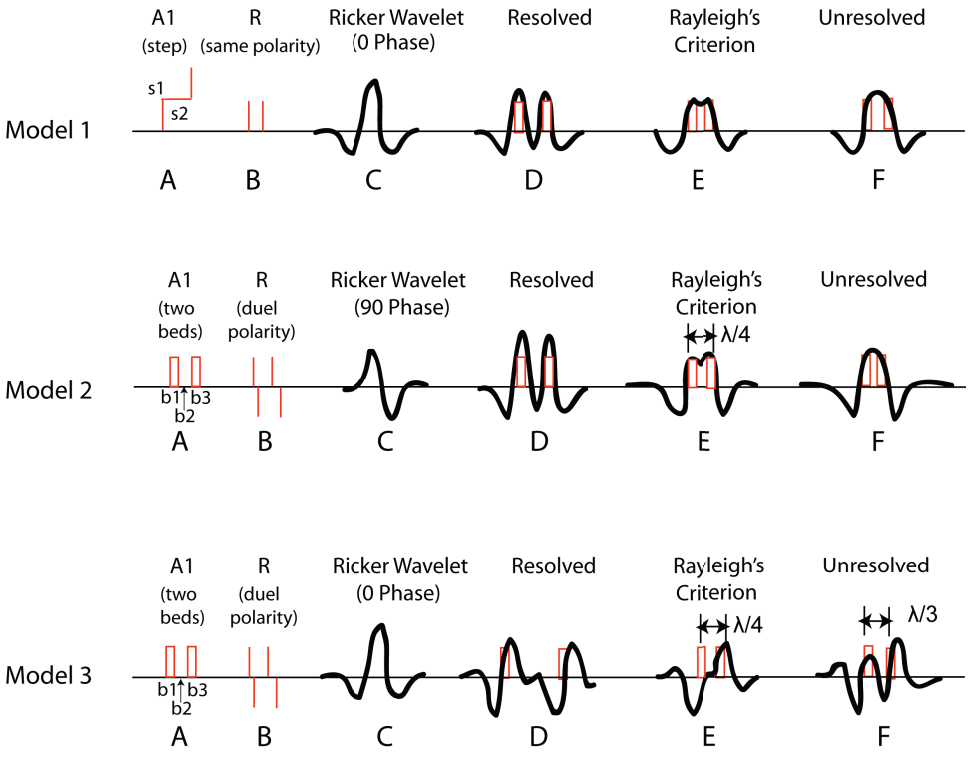

Fig. 2.10. Comparison of Rayleigh's criterion to a Ricker wavelet for thin beds [Zeng, 2009].

Model 1 describes the Ricker and Widess criterion for interfaces s1 and s2 where the beds reflectivity has the same polarity. Rayleigh's criterion can resolve the interface to $\lambda/4$; however, bed resolution from Model 2 and Model 3 are of more practical interest as there is a barrier bed, b2, inserted between beds b1 and b3. The polarities at top and bottom of each bed are opposite and when the wavelet phase is 90°, the resolution limit is $\lambda/4$. Model 3 is the same scenario as Model 2 except that the Ricker wavelet is 0° phase (corresponding to a symmetric wavelet). Rayleigh's criterion is unable to resolve the bed and results in a resolution limit of $\lambda/3$. This means that the resolution limit depends on the shape of the wavelet that is probing the thin-bedded structure. The figure shows that a 0° phase wavelet has a deteriorated bed resolution compared to a 90° wavelet [Zeng, 2009].

3. RICKER MODEL

As mentioned in Section 2.6, there are different criteria for describing the resolution limit. Resolution depends on the shape of the wavelet and is based on differences in amplitude. A model was constructed using an ideal Ricker wavelet with 0° phase in order to observe how amplitude and phase behaves as a bed thins. Figure 3.1 illustrates the ideal model for the merging of two Ricker wavelets of opposite polarity. Trace 1 is the signature of two Ricker wavelets that are greatly separated. Trace 7 is the signature as the beds begin to merge and constructively "add". Trace 8-10 shows the case in which the two wavelets are merged, thereby creating an interesting effect in the amplitudes. Trace 11 is the completely merged wavelet with double amplitude.

The colors in Figure 3.1 represent high amplitude (red) and low amplitude (blue). The color bar on the right of the figure displays the range of amplitudes from roughly 1.5–.5 in arbitrary units. The thinning bed is visually represented by the symmetric shape of a wavelet where the edges of the wavelet are zero, followed by a positive gradient in amplitude.

This model is used in the following to understand how radar waves might probe subsurface thinning beds in realistic situations. A phase and amplitude analysis of the idealized case shown here can provide insight into bed resolution derived from common-offset GPR data taken at the field site, Padre Island.

3.1 Spectral analysis

Using actual GPR data can be extremely challenging because of heterogeneity and noise. In order to extract information from the GPR data, trace windowing and filtering is performed. The same process was applied to the theoretical Ricker model to compare results for consistency.

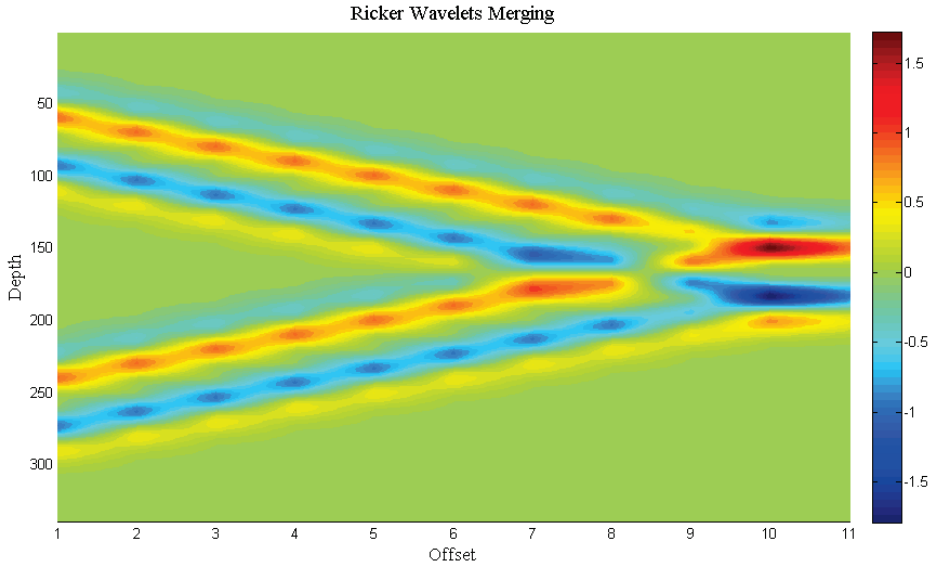

Fig. 3.1. 2D Plot of ideal Ricker wavelets merging together. From left to right, the beds begin separated and slowly merge together. Colors represent wavelet amplitudes where red is a high amplitude and blue is a negative amplitude.

3.1.1 *Windowing*

Windowing serves the purpose of removing discontinuities at the beginning and end of the data sequence that can distort spectral estimates [Everett, 2013]. In the present case, windowing is applied in order to center the wavelet within a specified window while preserving amplitude fluctuations near the endpoints of the trace.

The windowing method uses was a Hann window given by:

$$w[n] = \begin{bmatrix} \frac{1}{2}(1 - cos\frac{2\pi n}{M}) & 0 \leq n \leq M \\ 0 & otherwise \end{bmatrix} \tag{3.1}$$

where N is essentially the length of the window, and n is the integer values of the window sequence [Oppenheim and Schafer, 2010]. Simply put, the function multiplies each trace by a cosine curve where the center of the curve is a maximum of 1 (does

not change the value at that point) and the edges are zero. The center of the window coincides with the center of the data sequence

Figure 3.2 shows how effective the windowing is on real data. In this case, the windowing reduced the edges of the trace to zero, while roughly maintaining the values of the minimum and maximum amplitudes.

The windowing method was applied to all traces prior to performing the Fourier transform.

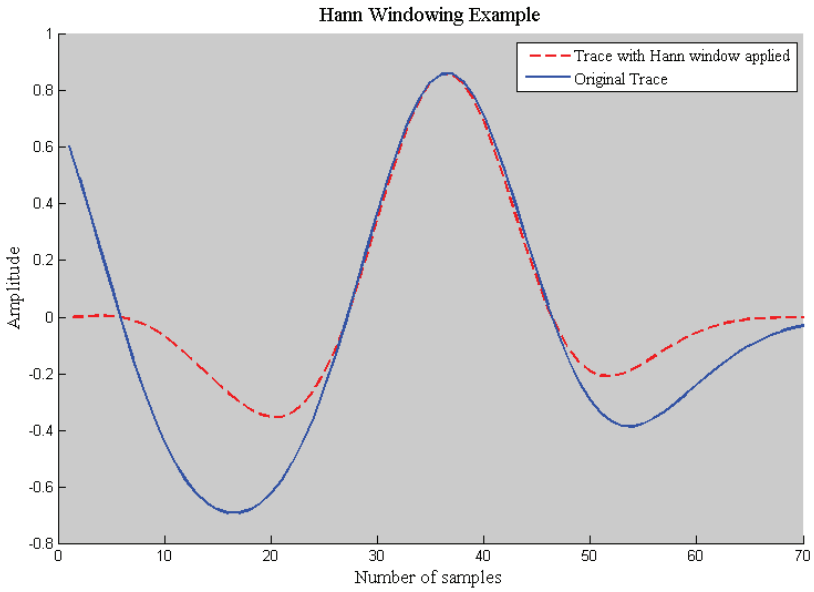

Fig. 3.2. Example of using Hann windowing on a real GPR trace

3.1.2 *Low-pass Filter*

A low-pass filter attenuates high frequency components of the data sequence. In Figure 3.3, the shaded blue area represents the high frequencies that are attenuated from a spectrum. Similarly, the area to the left of f1 would represent the action of a high-pass filter that attenuates low frequencies.

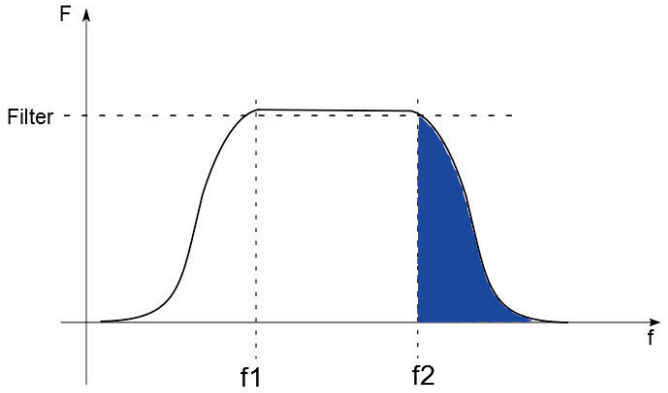

Fig. 3.3. Amplitude spectra of a bandpass filter. Blue shaded area represents the high frequencies attenuated from a spectrum. Modified from Ikelle and Amundsen [2005]

A low-pass filter, when applied to real data, removes much of the high frequency components and effectively "smooths" the trace (Figure 3.4). The red line represents the windowed original data and the blue line represents the low-pass filtered data. The filter generally maintains the shape and amplitudes of the trace while removing much of the fine-scale variability.

The specific style of filter used is the Butterworth filter with normalized cutoff frequencies between 0 and 1. The low-pass filter was applied to all GPR traces prior to performing the Fourier transform. The filter was also applied to the Ricker synthetic traces using a cutoff frequency of 0.1 and a 4th order iteration. The higher order correlates to a more abrupt cut-off: 1st order filter resembling a curved shape as in Figure 3.3 while a 5th order resembles a box-car.

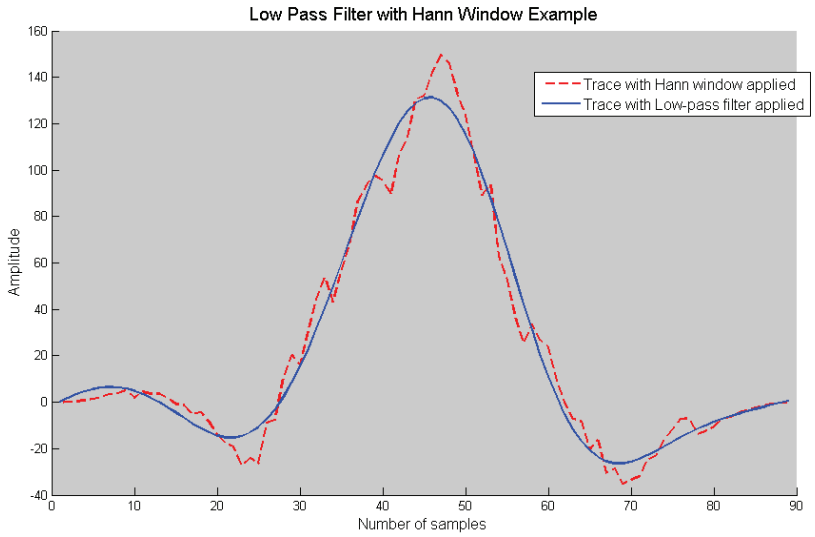

Fig. 3.4. Example of using a low-pass filter on a real GPR trace

3.2 Phase

The spectra of the synthetic Ricker traces is extremely sensitive to any slight variations from the original trace. An indication of the effect of slight fluctuations can be seen in the phase spectra. The phase, is measured in radians between $\pi/2$ and -$\pi/2$.

For the ideal case (no noise), the phase and amplitude spectra of the Ricker wavelet are seen in Figure 3.5.

The phase spectrum is symmetric because the Ricker wavelet can be split into even and odd portions. A Fourier transform can be expressed by a Fourier cosine transform and a Fourier sine transform (Equation 3.2).

$$F_x\,|X_k| = \int_{-\infty}^{\infty} E(x)cos(2\pi kx)dx - i\int_{-\infty}^{\infty} O(x)sin(2\pi kx)dx \tag{3.2}$$

where *E(x)* is the even portion and *O(x)* is the odd portion [Oppenheim and Schafer, 2010]. The phase is symmetric about $\frac{n}{2}$ where n is the number of samples.

For the ideal case, the phase has a distinctive "sawtooth" shape where it linearly increases to $\pi/2$ and then wraps to $-\pi/2$. For the complete Ricker model, two convolved Ricker wavelets merge to form a thinning bed. Figure 3.6 represents the amplitude at each trace as the wavelets merge. The Ricker wavelet is convolved with reflectivity spikes of the same polarity. In the case shown in Figure 3.6, the Ricker wavelet is convolved with reflectivity spikes of opposing polarity of two beds merging.

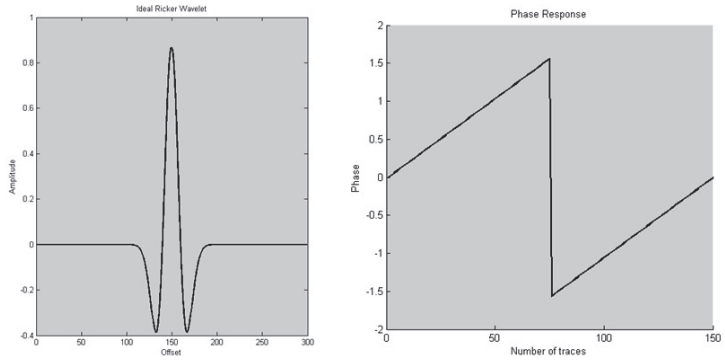

Fig. 3.5. The phase response (right) of an ideal Ricker wavelet (left).

It is unclear why the phase behaves the way it does for merging Ricker traces as beds (represented by reflectivity spikes) begin to merge; however, it is speculated that the phase is extremely sensitive to noise. When the wavelet deviates from the ideal case, any small variations in the amplitudes are noisy. This was determined by adding a random number to each sample of the Ricker wavelet. The values were extremely small; however the effect on the phase response resembled that of Trace 8. The solution to stabilize the phase spectra was to apply a low-pass filter. The phase response was expected to resemble the "sawtooth" shape; however when the filter was applied, the phase response then took on a different shape (Figure 3.7). The trace for which the beds began to merge was most affected by the filter and the phase spectrum has an anomalous slope, as indicated in more detail in the following sections. This is important to note when comparing the synthetic-trace results to real GPR data.

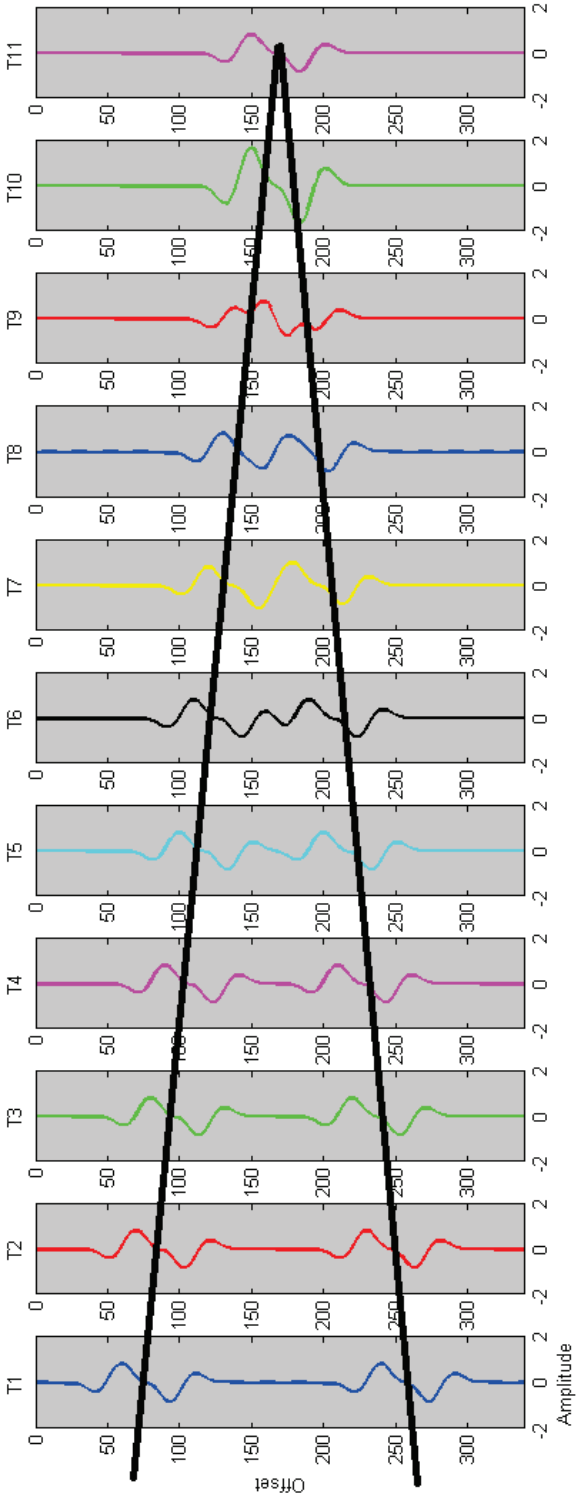

Fig. 3.6. Traces of the Ricker model.

3.3 Instantaneous Frequency

Though there were no apparent anomalous phase responses for the synthetic Ricker model, there was a trend from real GPR data. The instantaneous frequency represents an "attribute" of the data. Attributes are frequently analyzed in seismic data; however they are not studied as much for GPR data. In the case of GPR, the attribute is enhanced if the phase response has a small slope. In order to emphasize this characteristic, the instantaneous frequency is defined to be the inverse of the slope. A slope of zero will result in a high value of instantaneous frequency. Figure 3.8 shows that there is an increasing trend to the inverse slope as the beds merge together.

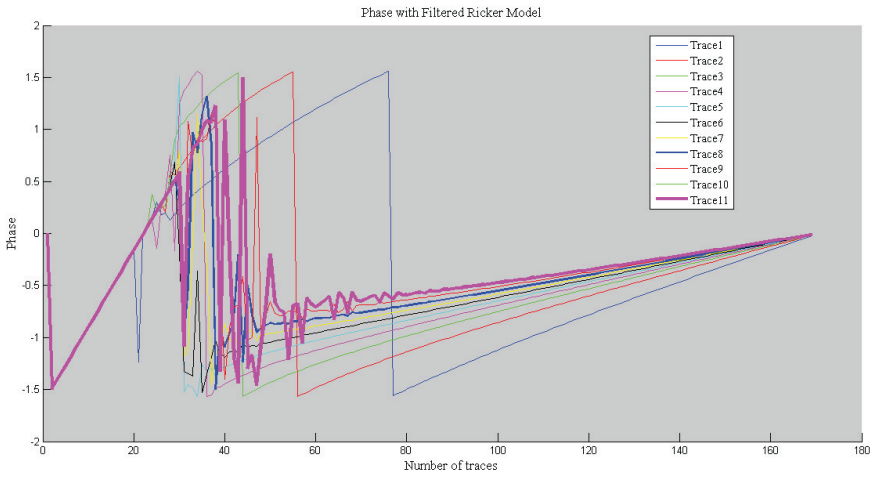

Fig. 3.7. The phase response of two ideal Ricker wavelets merging with a low-pass filter applied. The bold line (Trace 8) is when the beds merge together to form a double-amplitude Ricker wavelet.

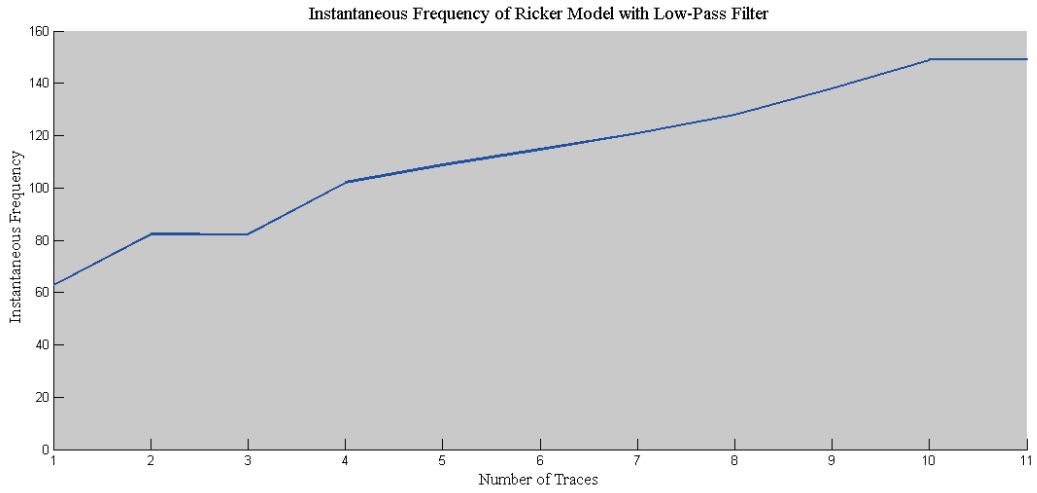

Fig. 3.8. The instantaneous frequency of the Ricker model with a low-pass filter applied.

4. FIELD STUDY

4.1 Equipment

The GPR equipment used for the field data acquisition is manufactured by Sensors and Software. The Pulse Ekko device is equipped with 200 MHz antennas, transmitter and receiver, fiber optic cables and a console unit. The console and attached laptop computer are run with a 12V marine battery whereas the transmitter and receiver are operated with 12-V sealed gel cells, as shown in Figures 4.1 and 4.2.

Fig. 4.1. Field setup of equipment. A car battery powers the console and data is collected with Toughbook laptop

Multiple survey designs were used to collect data with the 200 MHz frequency GPR unit. The first survey design used is called a common offset survey. In this design, the transmitter and receiver are maintained at a constant distance from each other and then moved at together along the profile with uniform station spacing. This method is reasonably fast to execute and easy to interpret. The second survey design incorporates a common mid-point (CMP) array. In this design, the distance between the transmitter and receiver change at each station. The result is a well imaged point in the subsurface but the data are time consuming to collect. Figure 4.3 is a sketch of two array configurations.

Fig. 4.2. Transmitter and receiver with 200MHz frequency antennas

The purpose of using two different arrays is to gain different perspectives on the subsurface structure. Both GPR survey designs were deployed at North Padre Island; however, the common-offset data will be used in the spectral analysis. The reason for using common offset is to gain a better visual representation of two-way travel time to the subsurface reflectors and to explore their lateral variability without spending excessive time to acquire the data.

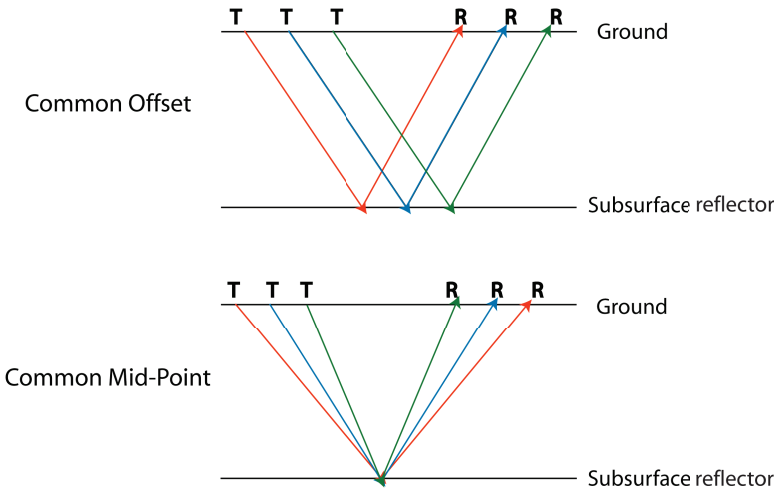

Fig. 4.3. Sketch of array configurations for Common Offset and Common Mid Point. Modified from [Neal, 2004]

The fixed distance between transmitter and receiver is 1.0 m and the array is moved in 0.1 m increments along the survey line. The separation between the transmitter and receiver depends on the frequency of the antennas used.

4.2 Site Description

Padre Island is one of the most southern islands along the Texas Gulf of Mexico coastline which extends from Corpus Christi to the Mexico border. Padre Island is a popular destination for vacationers but has been left fairly undeveloped because of legislation passed in 1962 preserving it as a National Seashore [Weise and White, 1980].

The beaches of Padre Island are only several thousand years old. Padre is a barrier island where the coast changes constantly [Weise and White, 1980]. The island is subjected to longshore currents, waves, eolian processes, sea-level rise and hurricanes [White, 1978]. The island was first separated from mainland Texas from heavy waves in the Gulf of Mexico, creating a lagoon which is now known as Laguna Madre. Over the last 20,000 years, sea level has risen about 120 m mostly due to glacial melting [Weise and White, 1980]. Incised river valleys deposited offshore bars, and as the sea level rose, the bars grew into segmented barrier islands. Over a few thousand years, the segments have joined to form a continuous barrier island. The old river valleys flooded and became the bays and estuaries that are currently seen along the Texas coastline [Weise and White, 1980]. The topography of Padre is shaped largely by prevailing southeast winds that build up foredunes which can reach as high as 6 m above sea level [Weise and White, 1980].

The present shoreline conditions are subjected to processes from wind currents, water processes like waves and currents, and land processes associated with vegetation and faunal activity. Waves and longshore currents interact with the shoreline to form offshore bars. The waves then eventually reach the beach where energy is released by eroding on land within a swash zone [Weise and White, 1980]. The surf zone

is a part of the forebeach that is constantly covered and uncovered by the swash and backwash of waves [Weise and White, 1980]. Waves can also be constructive where they deposit sand along the beach. The steeper the waves, the more destructive they are.

Once sediment is deposited on shore, wind picks up the particles and transports them landward. Most sediment is trapped by vegetation. However, looking at the landscape of Padre Island, there are many fore-dune ridges parallel to the Gulf of Mexico. The fore-dune ridges trap moving sediment so that it is deposited in the fore-dunes as opposed to moving to the back-dunes. The sand is temporarily trapped in the structure of the fore-dune; however, during a large storm or high tide, the sand can easily be transported back into the Gulf of Mexico [Weise and White, 1980].

Hurricanes and large storm systems build up in the Gulf of Mexico and can have devastating effects to the coastal regions of Texas. Some storms dissipate before reaching the shores of Texas; however the hurricanes that hit Padre Island, can create storm surges, strong winds, and washovers. During a storm, a large wave pushes down a foredune and spreads out in a fan-like shape, scattering sands, shells and vegetation.

Data were collected on North Padre Island National Seashore (27 27 37N, 97 16 59W) near Corpus Christi, Texas. The site was chosen based on permit availability, vehicle access, and interesting sedimentary depositional systems that included pinch outs. Figure 4.4 shows the location of data collection. Three dunes were analyzed at Site 1, Site 2, and Site 3.

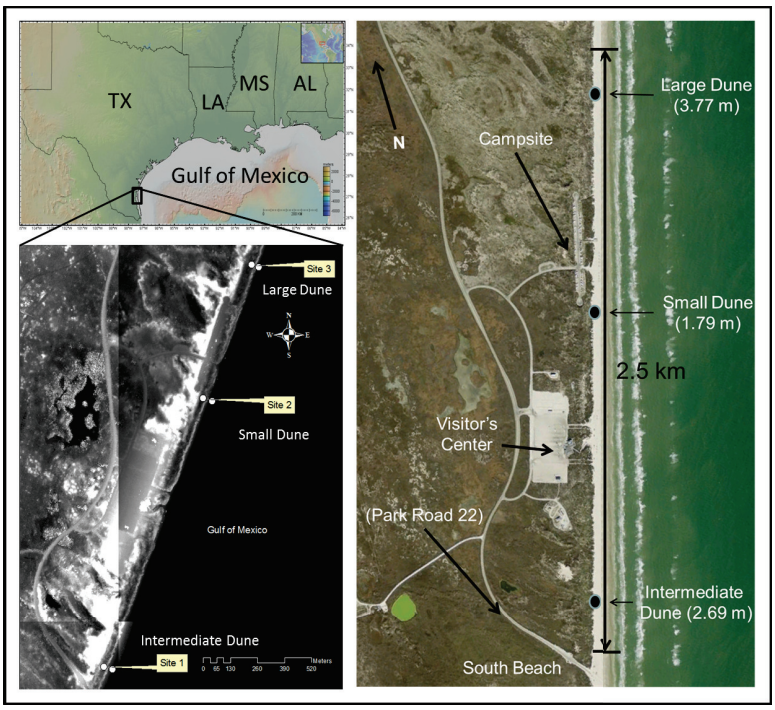

Fig. 4.4. All three data collection sites at North Padre Island. Site 1, intermmediate dune, Site 2, small dune, Site 3, large dune [Weymer, 2014]

4.3 Data Collection

GPR is a versatile technique that has been used in many environmental applications including near surface sedimentary processes like dune structure, and deposition of channelized sands Neal [2004]. These studies have been very successful at detecting minor heterogeneities in the subsurface. GPR was chosen because it is ideal for shallow investigations with high resolution.

Data were also acquired at North Padre Island from 2009-2011. The data used in the analysis was collected and processed by Brad Weymer, a PhD student at Texas A&M University. Acquisition was performed using 200 MHz frequency antennas in the TE mode at three different locations characterized by the presence of a small dune, intermediate dune, and large dune, respectively. Multiple lines were collected

at each site in order to image the internal structure of dunes. Figures 4.5-4.7 show the length and orientation of each line. Several trips were taken to Padre Island for data collection, resulting in a comprehensive suite of GPR profiles at each site.

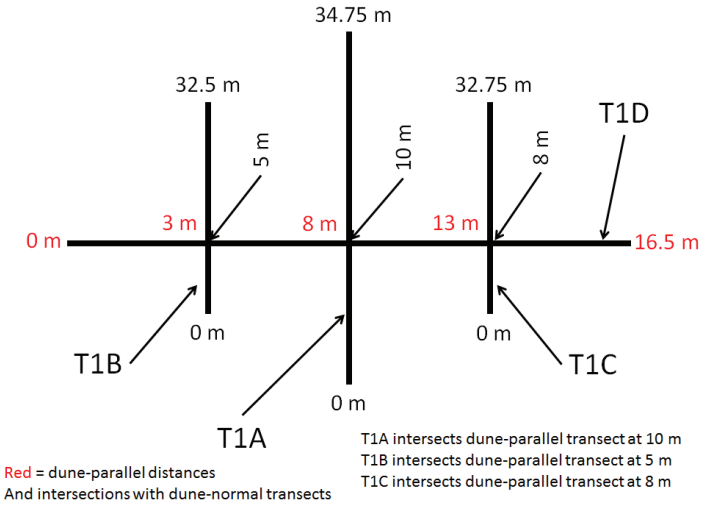

Fig. 4.5. Site 1, intermediate dune, data acquisition with orientation and lengths [Weymer, 2014]

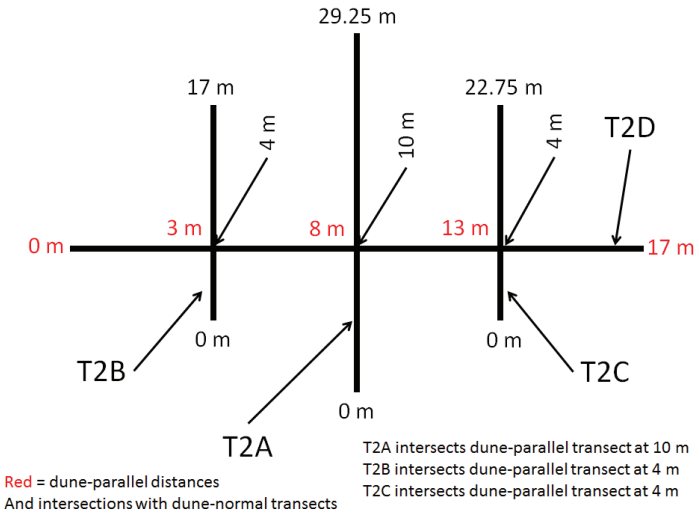

Fig. 4.6. Site 2, small dune, data acquisition with orientation and lengths [Weymer, 2014]

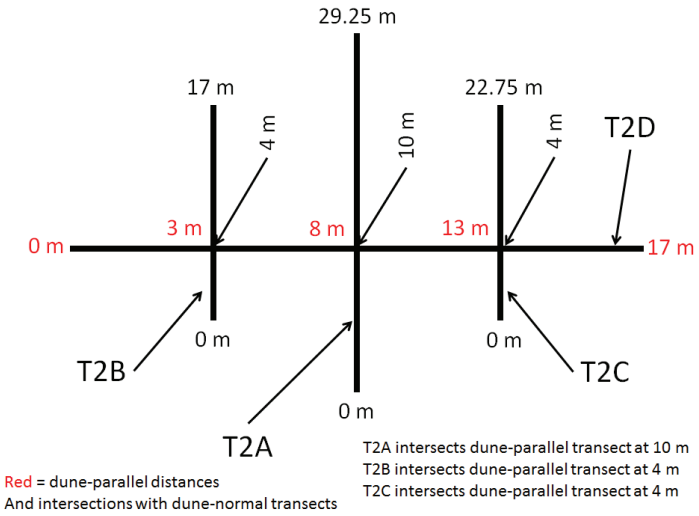

Fig. 4.7. Site 3, large dune, data acquisition with orientation and lengths [Weymer, 2014]

Fig. 4.8. Data acquisition at Site 3

4.4 Data Processing

Data processing is a required step in the interpretation of GPR data. The goal of data processing is to enhance the subsurface imaging of structures remaining true to the original data. Data from Padre Island were processed in a standard sequence using time-zero drift, dewow, background subtraction, migration, topography and automatic gain control (AGC). The processing was done in the order listed using Sensors and Software package Ekko View Deluxe.

The time-zero drift is necessary to indicate exactly where the first arrival is located on each trace [Neal, 2004]. The Pulse Ekko system requires the correction be made before data collection; however, the zero-time may drift as the survey proceeds. Accounting for the time-zero drift is essential because it otherwise can cause misalignment of the air wave, ground wave, as well as primary and secondary reflections [Neal, 2004]. The correction is done by shifting traces up or down by the required amount of time. The data were corrected with time-zero drift to ensure that the reflections near the surface is the first data being processed.

The early-time signal is often saturated because of the time interval between transmitter pulses during data collection as well as the large energy input from the air wave and ground wave [Neal, 2004]. The resulting low frequency "wow" trend is superimposed on the high frequency reflections [Cassidy and Jol, 2009]. Applying dewow is important because it reduces the data to a mean zero level through the application of a high-pass filter [Neal, 2004; Cassidy and Jol, 2009]. Figure 4.9 shows how the GPR trace is corrected using a dewow filter which removes the low frequency bias and centers the trace on the axis.

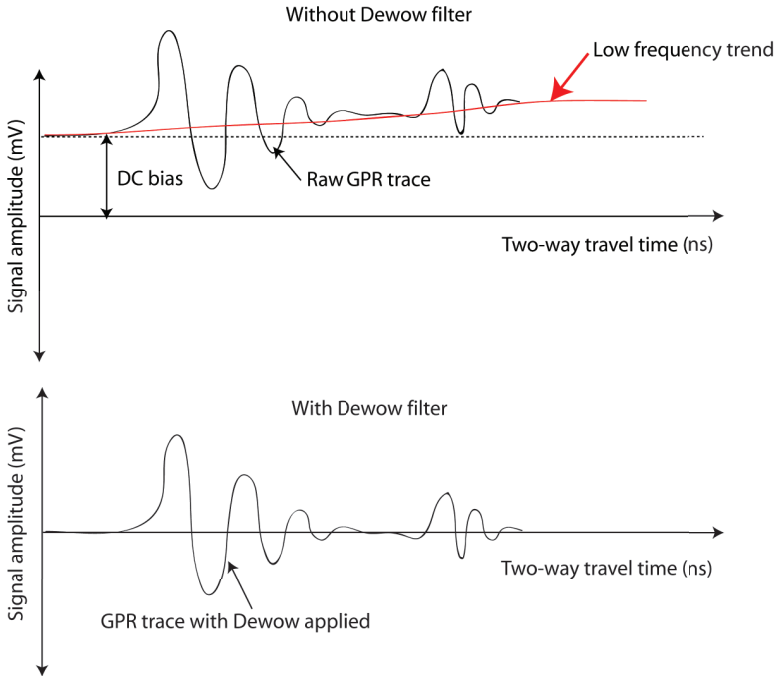

Fig. 4.9. Dewow filter correction on original GPR trace. Modified from Cassidy and Jol [2009]

The background subtraction filter removes background noise by taking the mean radar amplitude of all traces and applying it to each trace [Cassidy and Jol, 2009]. The filter removes unwanted ground clutter from laterally continuous signals [Everett, 2013]. This is especially important for data collected in lossy materials where shallow near-surface layers can cause strong reverberation signals [Cassidy and Jol, 2009]. One of the drawbacks to using a background subtraction filter is that it can remove the signature of a continuous flat-lying reflector such as top of bedrock of the water table [Cassidy and Jol, 2009; Everett, 2013].

Migration was originally developed for seismic interpretation. Migration is an image restoration technique where the objective is to resolve the true geometry of various reflectors in the subsurface [Ikelle and Amundsen, 2005]. The use of migration in GPR is not as successful as in seismic because of the complexity and heterogeneity

of most near-surface applications [Cassidy and Jol, 2009]. Cassidy and Jol [2009] list some limiting factors that inhibit using migration in GPR:

- The velocity structure of the subsurface must be estimated. In our case, a velocity analysis was performed using a common mid-point (CMP) profile. The average velocity value for the data was v=0.12 m/ns. A more accurate migration could be performed using a multi-layered velocity profile. The subsurface materials at North Padre Island are fairly homogeneous so that only one velocity value was used.

- The source is spatially uniform and propagates spherically. As mentioned in Section 2.2, a wave travels radially outward from the source [Annan and Butler, 2005]. This neglects the details of the radiation pattern, which is not spherical.

- The far-field conditions of a radial, uniformly propagating scalar field are assumed. The radiation patterns at the far-field were discussed in Section 2.4.2.

- Data are collected in normal incidence or monostatic mode.

- No dispersion or attenuation is considered. The assumptions and problems with attenuation were discussed in Section 2.4.1.

After applying the migration process, the GPR sections are much easier to interpret because diffractions are removed and reflectors are placed back in their correct spatial locations [Annan, 1999].

Typically, datasets are collected over uneven ground with varying topography. A correction is also required to reposition the data to its correct spatial context [Cassidy and Jol, 2009]. The correction "shifts" the acquired radargram to the correct elevation (Figure 4.10). The same velocity value used for migration was also used for the topography correction. The correction was performed by using elevations taken by a total station. It is especially important in our case to apply topography corrections because the variations in elevation are significant at sand dunes.

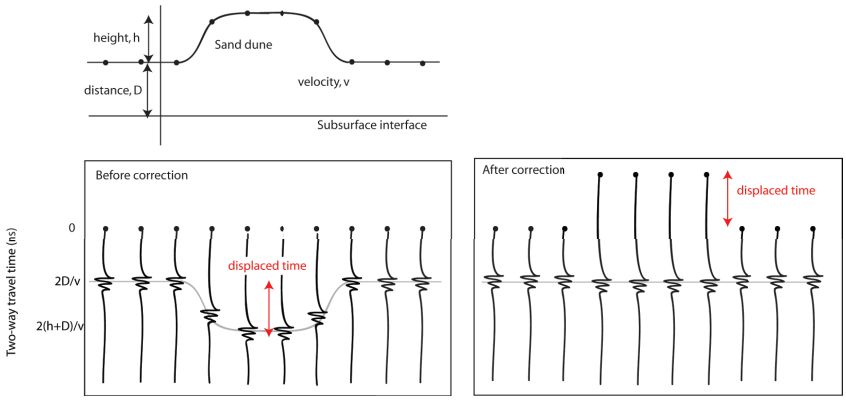

Fig. 4.10. Topography correction where traces are "pulled up" to the correct elevation. Modified from Everett [2013]

An automatic gain control (AGC) is a process that improves the visual form of the GPR section [Cassidy and Jol, 2009]. The purpose of the AGC is to equalize the signal at all depths to amplify weaker events. The AGC is inversely proportional to the signal strength [Everett, 2013]. Figure 4.11 displays how the AGC enhances the weak reflectors of a raw trace. An AGC was applied to the data with a window size of 250. The window size is important because if the window is too small, it can amplify noise as well as the signal; if the window is too large, the high-amplitude pulses dominate the calculation [Cassidy and Jol, 2009]. During data acquisition, a permanent gain is already applied; however, in the processing stages any further gain that is applied is a non-permanent change.

4.5 GPR Data Interpretations

Brad Weymer processed and interpreted the GPR data in terms of the internal structure of sand dunes. The interpretations identify interfaces between swash bars, storm surfaces, beach deposits, dune core, and rearslope accretion. The interfaces were identified visually from high amplitude reflections. Additional previous research has been done identifying dune structure using GPR (see Bristow et al. [2000] and

Bailey and Bristow [2000]) which influenced sedimentological and geomorphological interpretations on the structure of a sand dune.

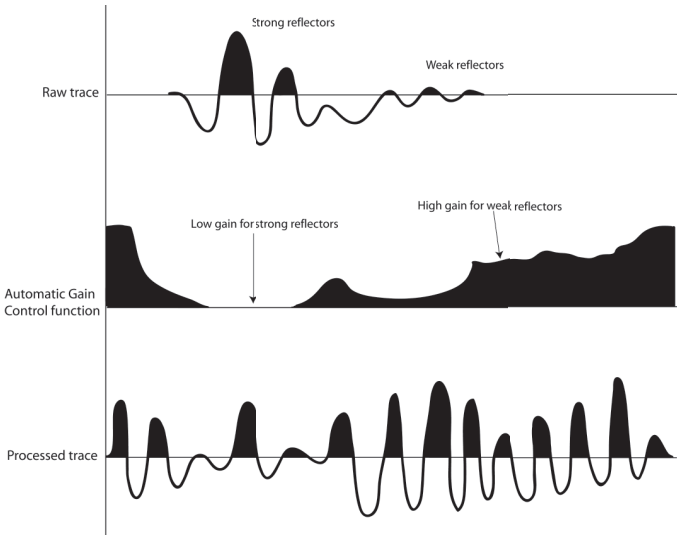

Fig. 4.11. Automatic Gain Control function applied to a raw trace. The weak reflections are amplified [Everett, 2013].

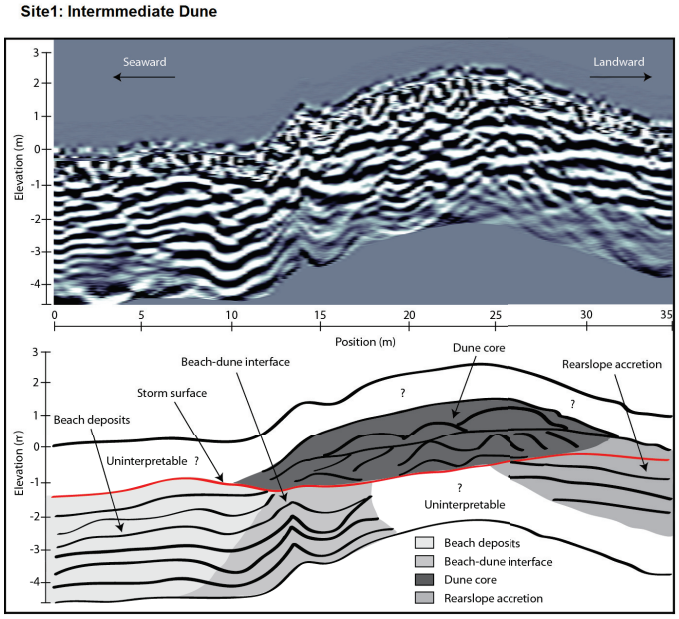

Fig. 4.12. Site 1 interpretation from processed GPR data [Weymer, 2014].

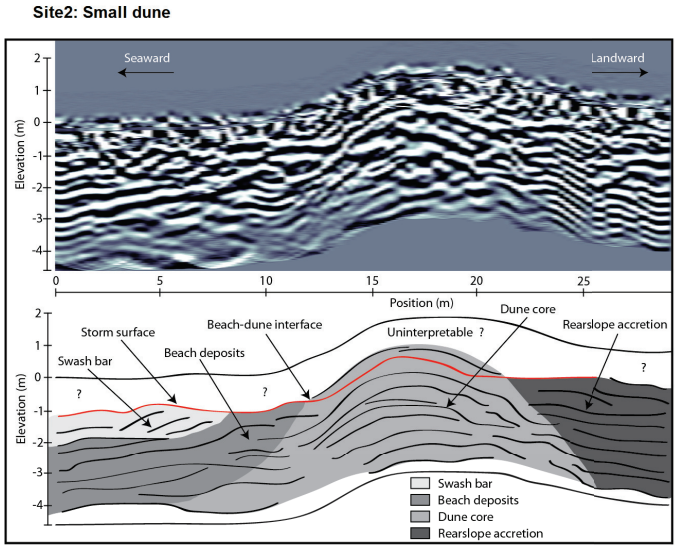

Fig. 4.13. Site 2 interpretation from processed GPR data [Weymer, 2014].

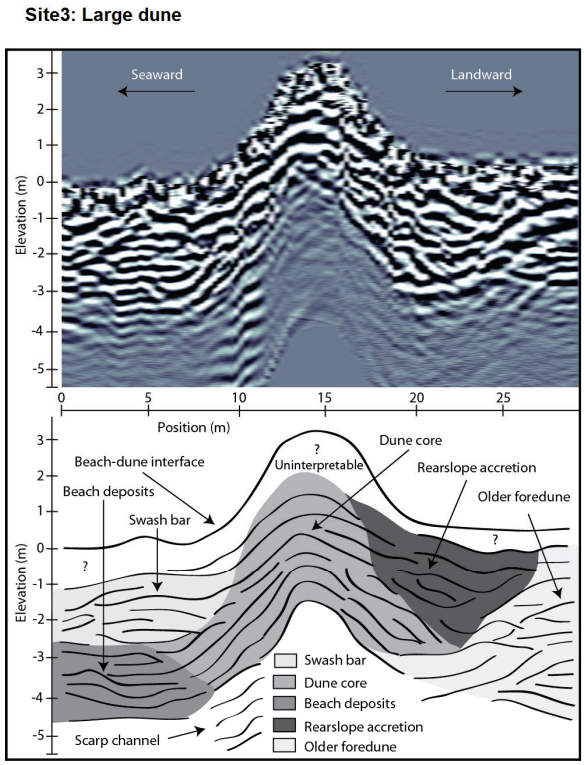

Fig. 4.14. Site 3 interpretation from processed GPR data [Weymer, 2014].

The GPR interpretations are very subjective and somewhat arbitrary based on the quality of GPR data. The spectral analysis here results in a more quantitative and objective interpretation of subsurface interfaces.

4.6 Spectrum Analysis

A Fourier analysis shows variations in amplitude and phase for a GPR trace. In some cases, the analysis reveals an anomalous phase and amplitude, which may correspond to an interface between two zones or detect sites where a bed pinches out.

The GPR traces were windowed and filtered, as described in Section 3.1. These two processes removed most of the noise associated with the GPR data. The Butterworth low-pass filter was applied using a 4th-order approximation with a cutoff frequency of 0.1. These values remained constant throughout the analysis to facilitate a consistent comparison of phase responses from different traces.

The windowing has a small effect on the resulting trace; however its effect is not as great as that of the low-pass filter. For real data containing high-frequency noise, the filter can greatly influence the resulting trace.

The filter removes a large amount of noise; however the phase is greatly affected by a low-frequency signal components. The phase response shows noise at low frequencies which is attributed to the fact that the filter removes only high-frequency content.

The first data example is from Padre Island at Site 1 where data were collected along an east-west profile along the of the dune. The traces were recorded at 21-24 m offset with elevation of about 1.0 -1.8 meters. Figure 4.15 shows the original GPR trace while Figure 4.16 shows the windowed and filtered data.

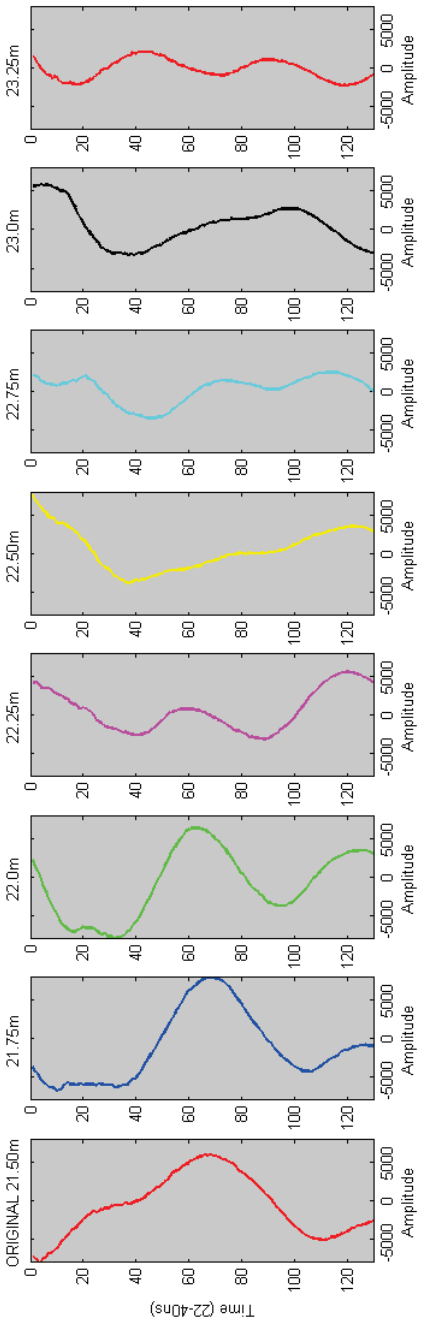

Fig. 4.15. Site 1, T1A 21-24, Original GPR traces

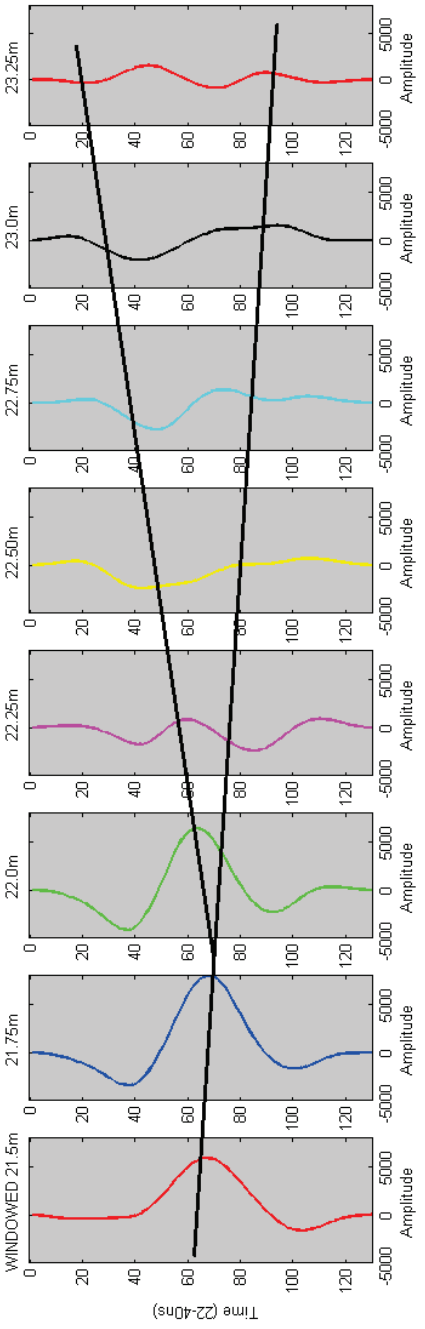

Fig. 4.16. Site 1, T1A 21-24, Windowed and Filtered GPR traces

Applying the spectral analysis reveals an anomalous phase for locations where the beds merge. This occurs at Trace 2 where the wavelet shape resembles that of a Ricker wavelet. At this point, the beds merge and the GPR response shows an increase in amplitude. The phase response (Figure 4.17) of Trace 2 is considered to be anomalous because it has a slope of about zero. In order to emphasize this attribute, the instantaneous frequency was represented as the inverse of the slope (Figure 4.18). This plot displays the inverse slope for each trace, and it should be noted that a spike is observed at Trace 2. This shows that a useful attribute to detect merging beds is the inverse slope of the high-frequency phase response.

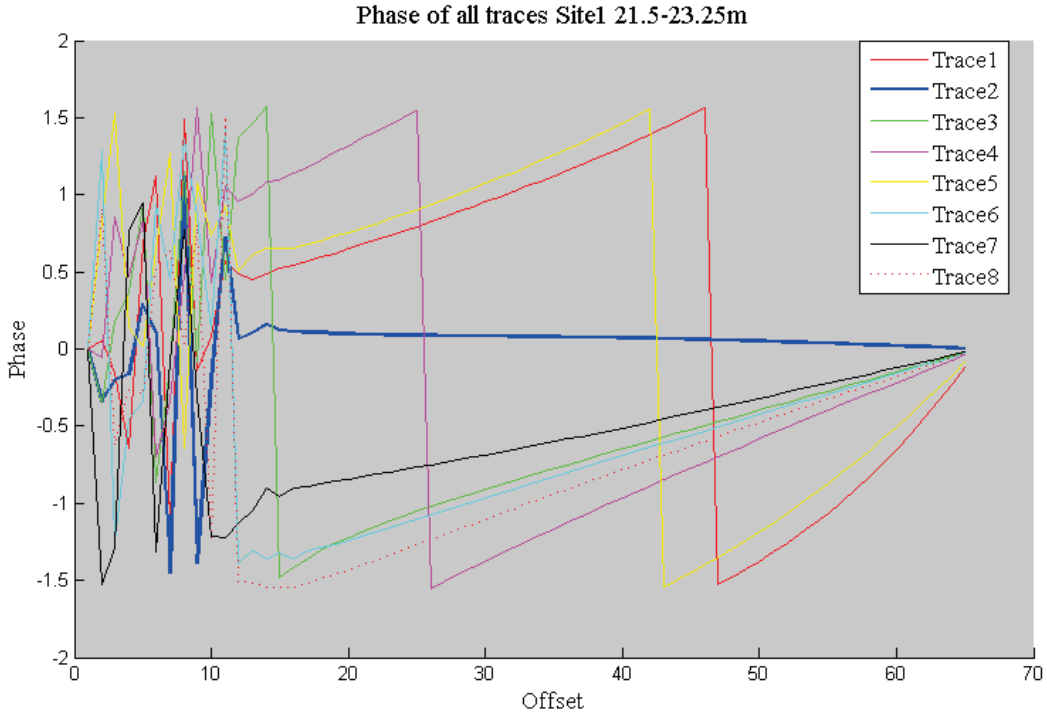

Fig. 4.17. Site 1, T1A 21-24, Phase response of windowed and filtered data

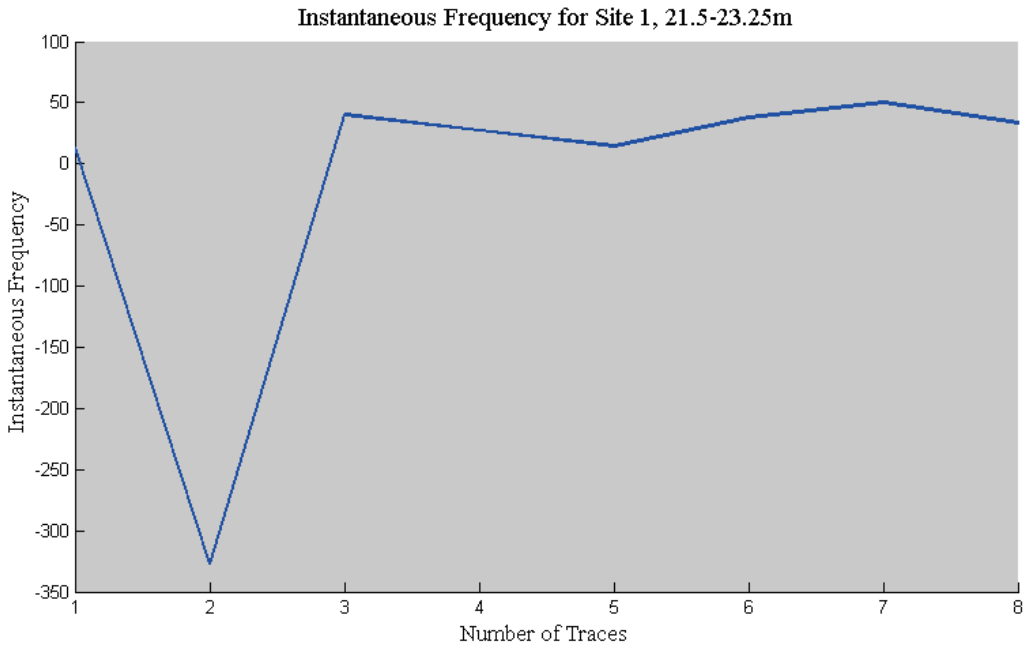

Fig. 4.18. Site 1, T1A 21-24, Instantaneous frequency from phase

The same phenomenon is observed for a second field example from Padre Island Site 2. The traces were selected at 6-8 m along-profile distance and depth of about 1.0 -1.7 m below the surface. Figure 4.19 shows the original GPR trace while Figure 4.20 shows the windowed and filtered data along with interpreted beds. The lines drawn ontop of the trace indicate the interpreted bedding merging.

Applying the spectral analysis shows an anomalous phase for beds such as Trace 3. The phase response (Figure 4.21) of Trace 3 is again anomalous because it has a slope of about zero. For Trace 3, the instantaneous frequency attribute (Figure 4.22) shows an anomalous peak.

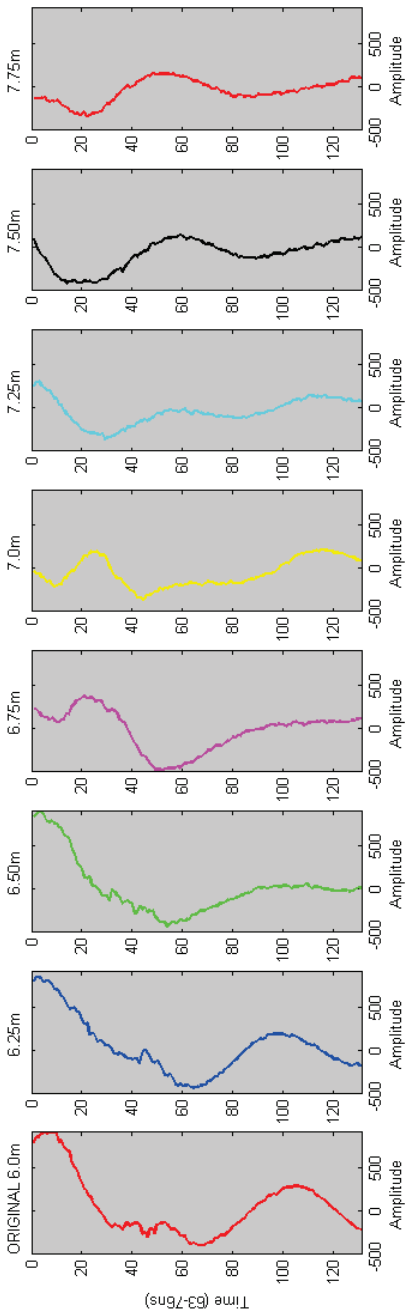

Fig. 4.19. Site 2, T2B 6-8, Original GPR traces

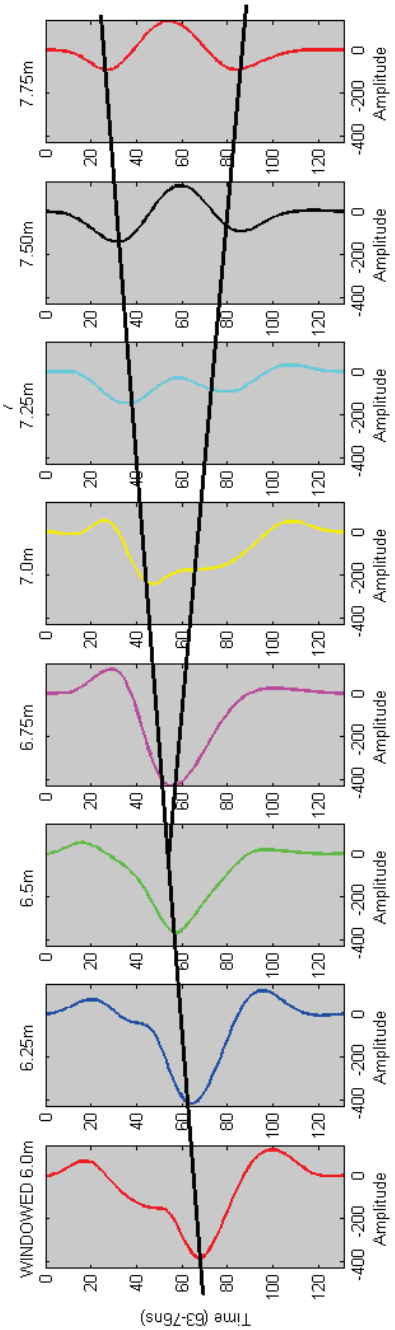

Fig. 4.20. Site 2, T2B 6-8, Windowed and Filtered GPR traces

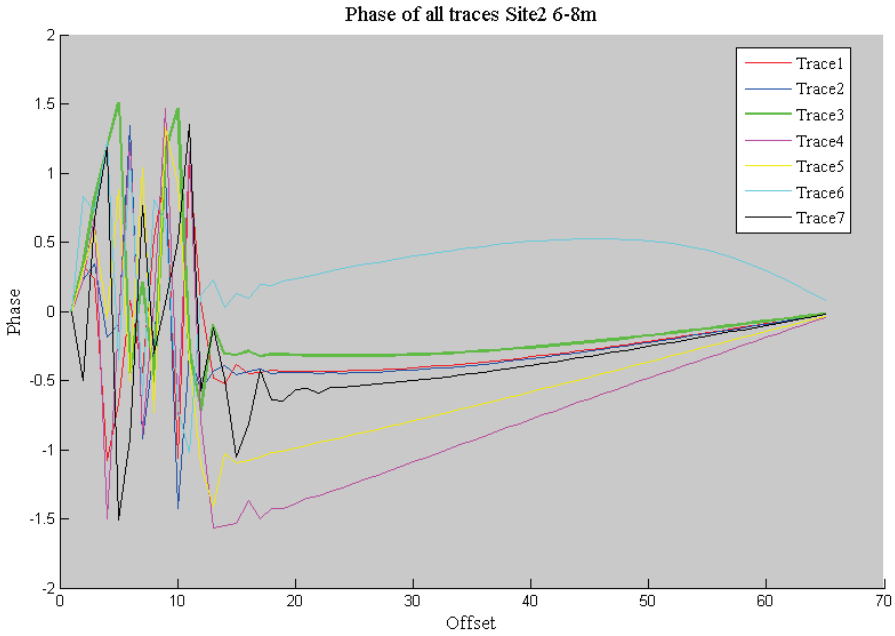

Fig. 4.21. Site 2, T2B 6-8, Phase response of windowed and filtered data

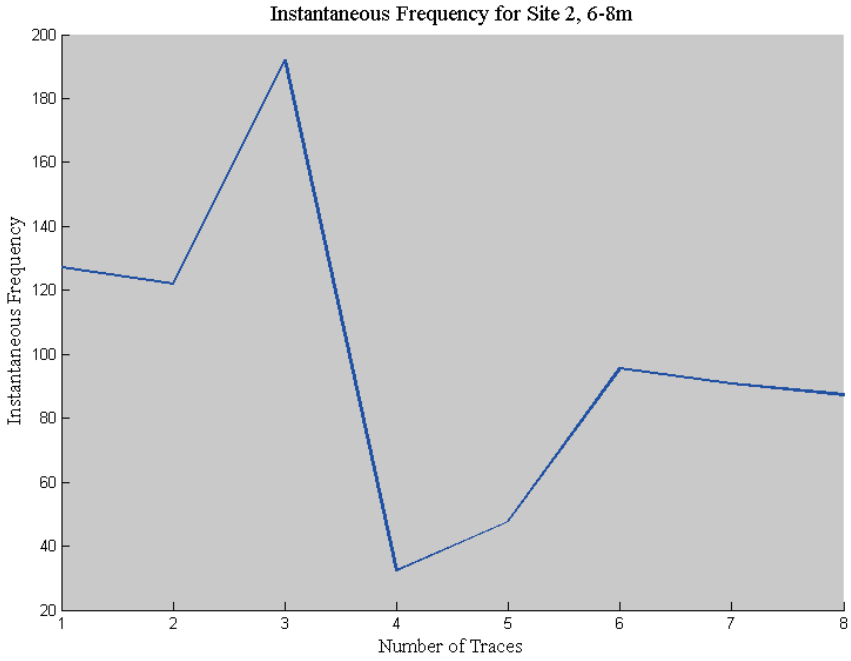

Fig. 4.22. Site 2, T2B 6-8, Instantaneous frequency from phase

The third data example is from Site 3. The traces were selected from along-profile distance 11-12m offset and elevation of about 1.1-0.2 meters above the surface. Figure 4.23 shows the original GPR trace while Figure 4.24 shows the windowed and filtered data with interpreted beds.

Applying the spectral analysis again shows an anomalous phase for locations associated with merged beds. This occurs at Trace 3. The phase response (Figure 4.21) of Trace 3 is anomalous because it has a slope of about zero. For Trace 3, the instantaneous frequency attributes (Figure 4.22) again peaks at a much higher level than the others.

The last data example is from Site 1 where the beds are not merging. The traces were selected from 28-32 m along-profile distance and elevation of about 1.5-0.3 m above the surface. Figure 4.27 shows the original GPR trace while Figure 4.28 shows the windowed and filtered data with interpreted beds.

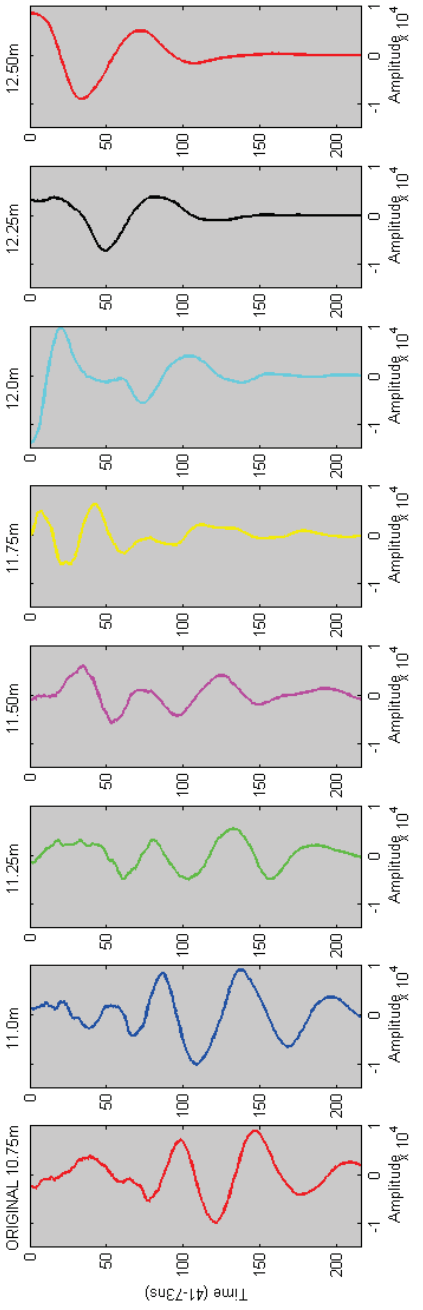

Fig. 4.23. Site 3, T3B 11-12, Original GPR traces

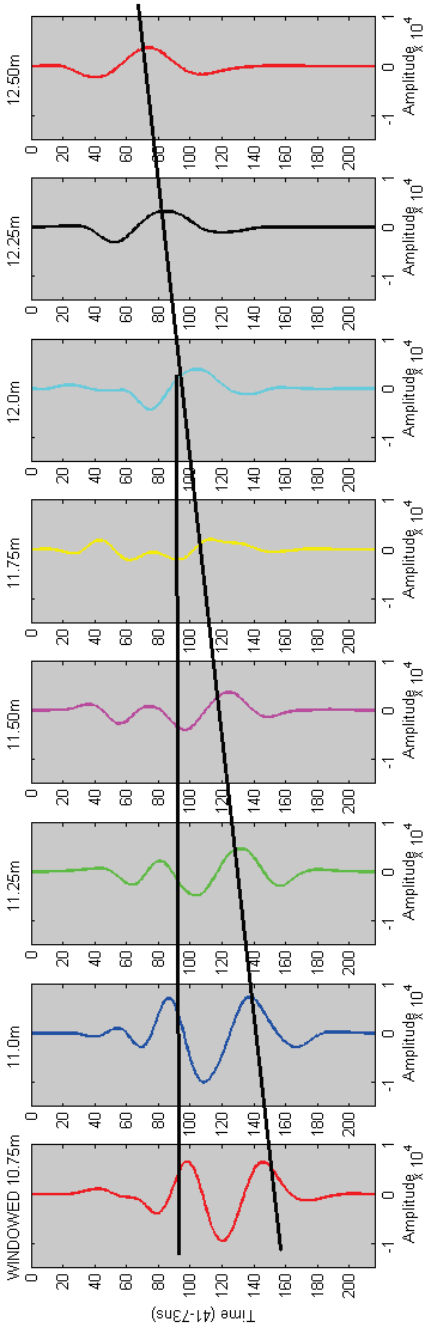

Fig. 4.24. Site 3, T3B 11-12, Windowed and Filtered GPR traces

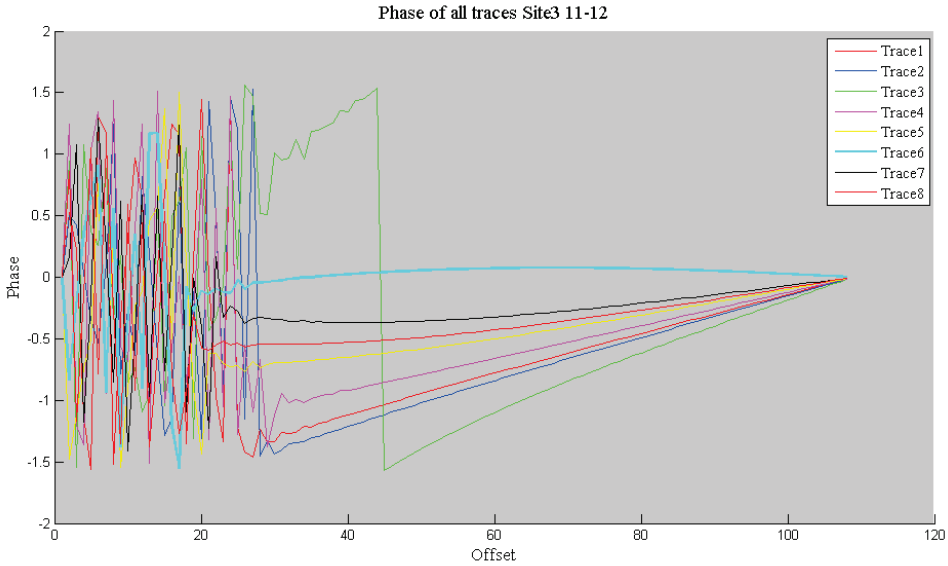

Fig. 4.25. Site 3, T3B 11-12, Phase response of windowed and filtered data

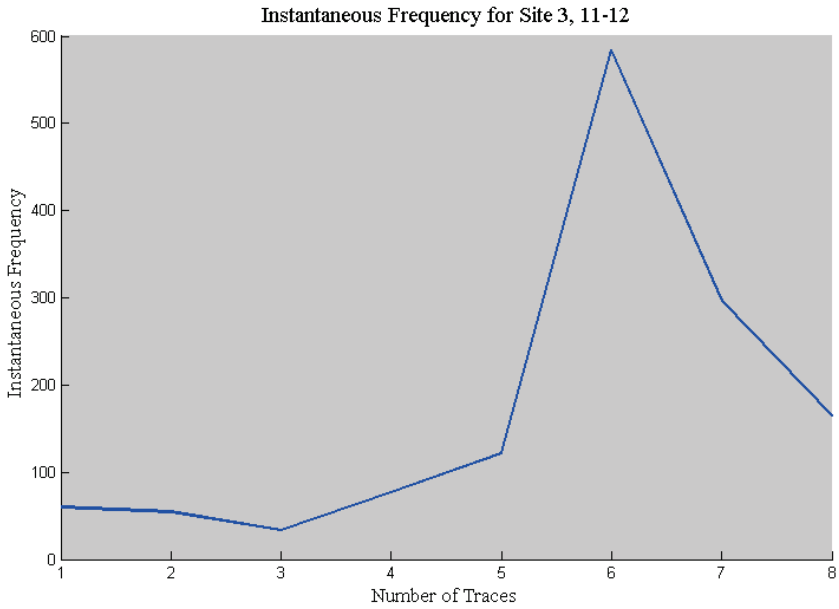

Fig. 4.26. Site 3, T3B 11-12, Instantaneous frequency from phase

Applying the spectral analysis for this scenario does not reveal an anomalous response. This data section was chosen to show how the attribute associated with horizontal reflectors is not anomalous. The phase response appears to be similar to previous examples, however the instantaneous frequency does not show an anomalous response associated with a near-zero slope. The phase response (Figure 4.29) of Trace 6 is slightly anomalous however the trace appears to be noisy even with the applied filter. The instantaneous frequency attribute (Figure 4.30) is scattered with a large range of values. There is not one trace in particular that shows an attribute that is significantly greater than the those of other traces.

The field data examples showed that an anomalous a phase response of near-zero slope occurs at locations associated with merging. The anomalous attribute was emphasized by taking the inverse of the slope. This interpretation is also consistent with the field example in which beds do not merge; the phase response was not anomalous.

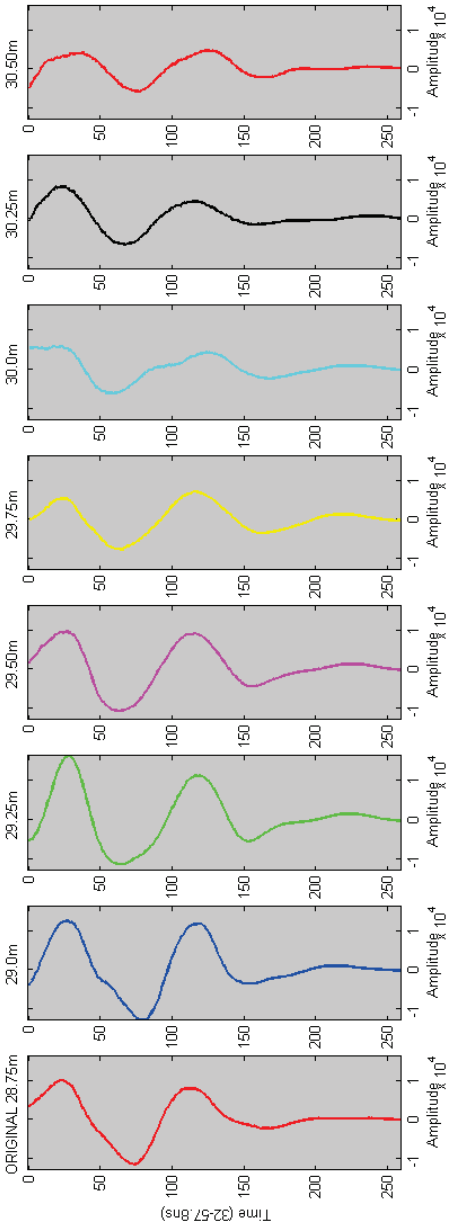

Fig. 4.27. Site 1, T1A 28-32, Original GPR traces

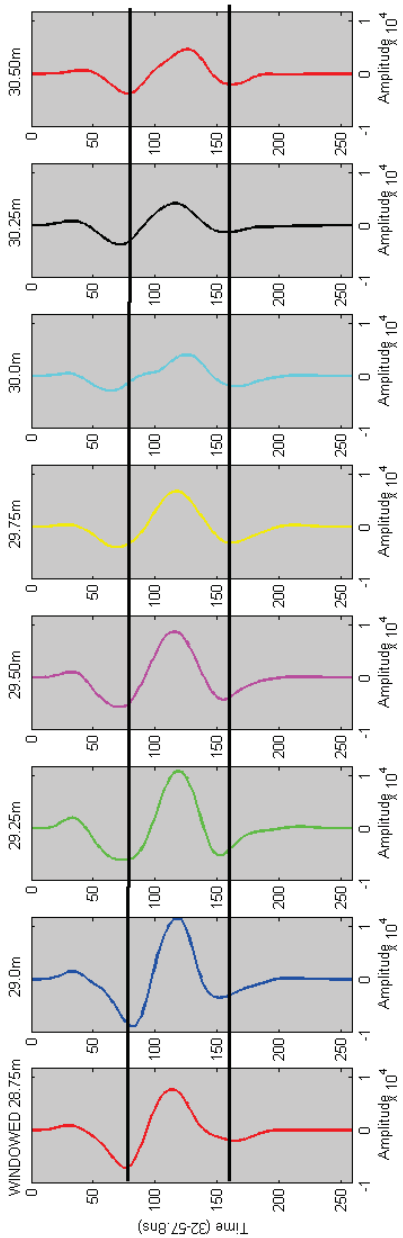

Fig. 4.28. Site 1, T1A 28-32, Windowed and Filtered GPR traces

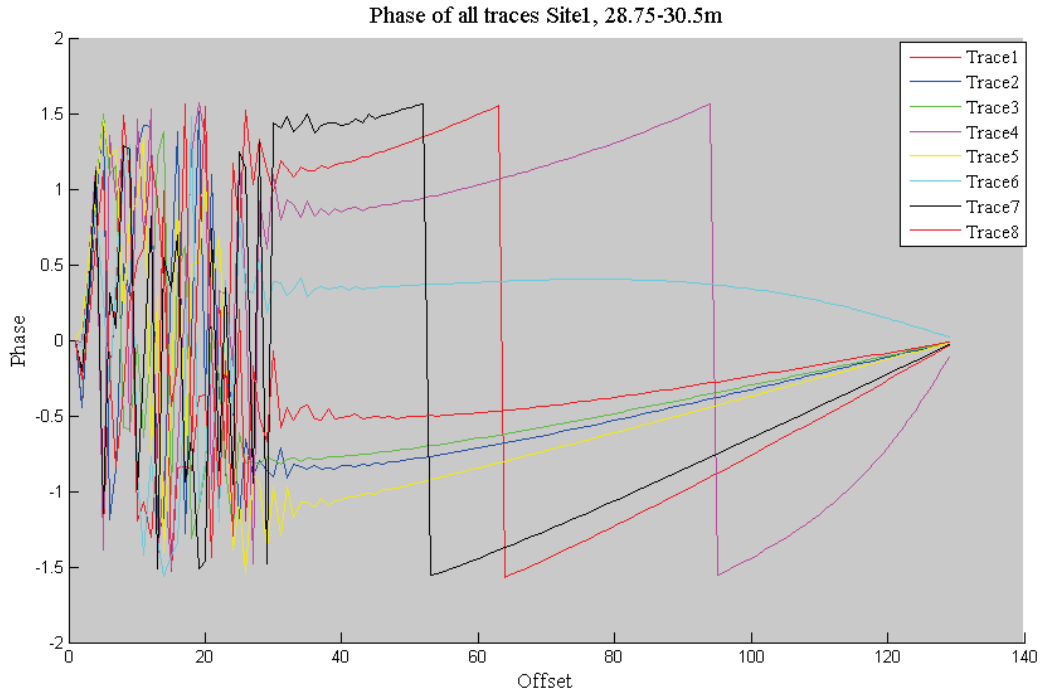

Fig. 4.29. Site 1, T1A 28-32, Phase response of windowed and filtered data

Fig. 4.30. Site 1, T1A 28-32, Instantaneous frequency from phase

5. DISCUSSION

Dielectric constants are almost entirely dependent on water content and increase with depth into the vadoze zone pproaching the water table. This is an important consideration to make when determining whether or not the anomalous features as a result of spectral analysis are in fact caused by variations in soil mineralogy or water content. There is a direct relationship between reflection amplitudes and soil hydraulic properties; however, it is not possible to obtain a direct derivation of water content from GPR amplitudes [Schmalz and Lennartz, 2002]. To estimate water content in the subsurface, cores should be taken where the samples are weighed before and after drying.

Equation 2.5 is the amplitude reflection coefficient for a two layer system. To compare the amplitude reflections when approaching the water table, $\epsilon_1 = 5$ and ϵ_2 increased from 10-80 approaching the water table. Figure 5.1 is the plot of reflections increasing with water content.

The reflections are very strong when ϵ_2=80, which is the dielectric constant of water. There are three shaded regions; the first is the vadose zone followed by the capillary fringe, and lastly, the water table. The amount of water increases as you approach the water table. The vadose zone and capillary fringe are a result of an unconfined aquifer where the water table is not limited to a specific interval in the subsurface. The vadose zone will fluctuate in the field from rainfall, sea-level rise, or drought conditions.

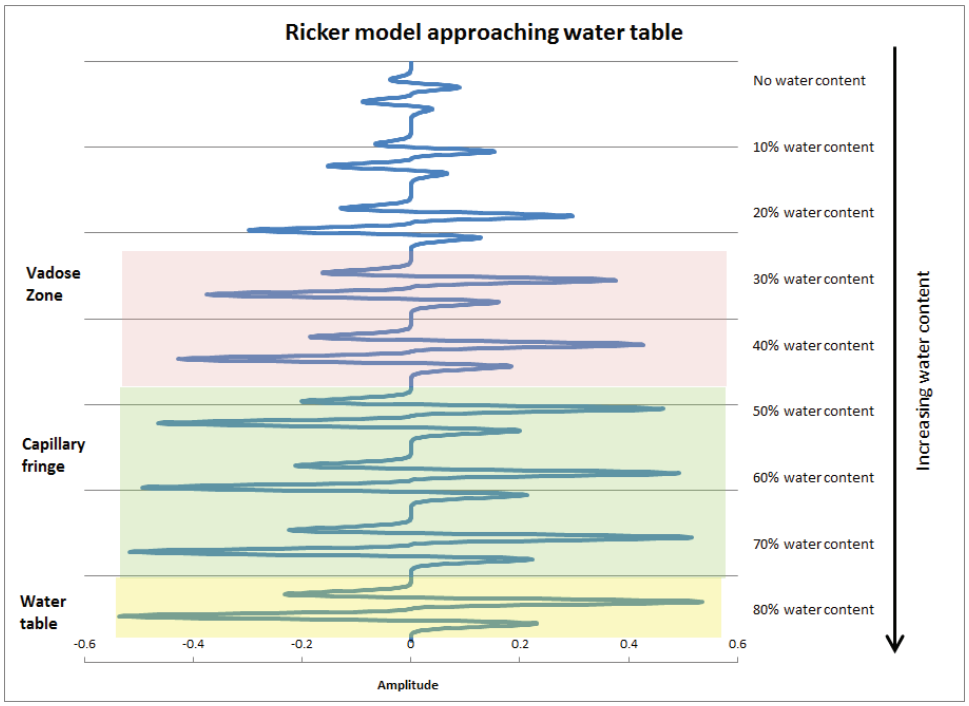

Fig. 5.1. Convolved Ricker model reflections approaching the water table

The Ricker model with incorporated water content information is a first look at how reflection amplitudes can be heavily influenced from the amount of water in the subsurface. To validate that the spectral analysis was observing merging beds as opposed to fluctuations in water content, coring information from Padre Island near the field sites will be used.

5.1 Analysis of Coring from Padre Island

Coring was done at each field site in order to gain information of the first meter into the subsurface. This was to compensate for the quality of GPR data at the surface because of the effect of the air wave and ground wave. The cores were taken using a Vibracore system and then scanned in high resolution using equipment at the IODP (Integrated Ocean Drilling Program) labs at Texas A&M University. The scans were able to show slight variations in coloration, which can be useful for

estimating water content. At the time of splitting, water content analysis was not done; however a grain size analysis was performed.

The water table is not clearly identified because coring was taken to approximately 1.5 meters in depth; however it is hypothesized that the water table is close to the surface due to proximity to sea level [Weymer, 2014].

Since water content is not known, one way to verify the spectral analysis is to observe beds further from the water table. Site 3 is the best dataset to use because the dune is the most elevated where amplitude reflections will be less influenced by water content. Figure 5.2 is a diagram of where the cores were taken along the dune profile. Cores A-C were taken seaward side at a lower elevation. Core D was taken on the back side of the dune and was taken at a higher elevation. There is some discoloration in Cores A and B that might indicate water presence; however there were other organics present at the same depth. The discoloration occurs at approximately 0.8m depth, which is fairly close to the surface and would be consistent with the depth of the water table because the core was taken on the seaward side.

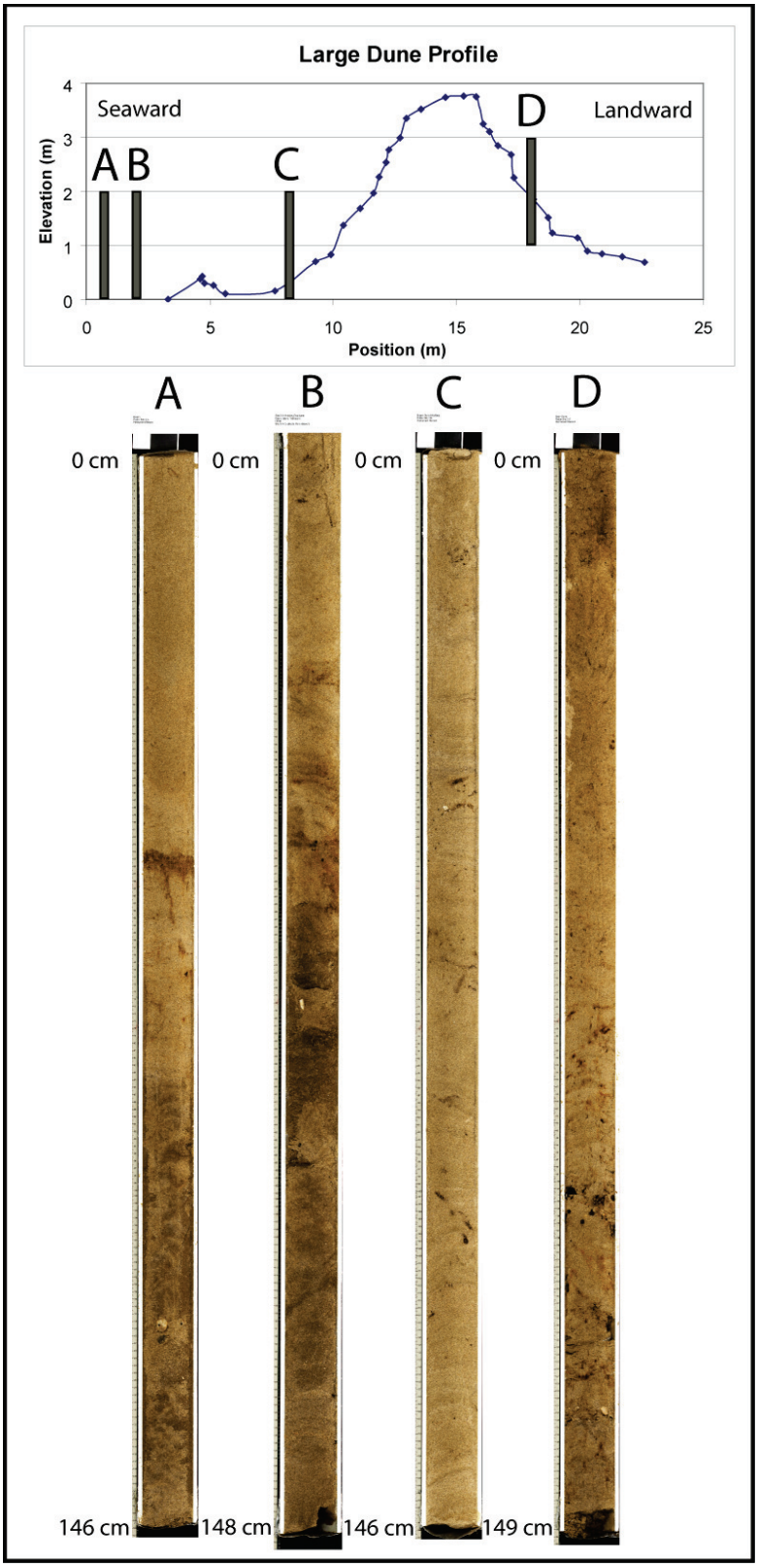

Fig. 5.2. Diagram of the cores taken at Site 3 [Weymer, 2014].

Looking at Core D in particular, the sorting is relatively consistent until a shell hash layer at 1.1 m and 1.3 m depth. Figure 5.3 is the grain size distribution for Core D. Assuming the water table is fairly close to sea level, the elevation of Core D would not intersect the water table because the core was taken higher up on the dune topography and was only about 1.5 meters in depth. The slight variations in color from Core D appear to be organic matter [Weymer, 2014]. The depth of Core D is about the same depth as the spectral analysis example from Site 3. This provides some validity that because the water table is near the surface, but not as high as the dune elevation, the spectral analysis from Site 3 is likely indicating a slight variation in soils as opposed to water content. It is likely that the dielectric contrast is from organic material, shells, or small variations in soil.

This argument may not be completely valid for the spectral analysis from Site 1 and Site 2 because the examples were closer to sea level. With that said, variations in dielectric constants are related to water content. It is difficult to definitively state whether the spectral analysis anomalies are where beds merge or where water content is varying.

The amplitude reflections of the field examples were on similar scales to one another. If one had a much higher amplitude reflection, it could be inferred that it had a greater water content. Since they have similar amplitudes, it is assumed that the merging beds have similar water content and are observed to merge from slight variations in soil properties such as grain size or sorting.

Applying a spectral analysis to traces that border the intersection of Core D do not show any anomalous features of pinch outs. It is difficult to visually find an area from the GPR data so close to the surface that would have merging beds because resolution is lost from the air wave and ground wave interference. Core D has varying discoloration from organic material at roughly 1 m depth. This was interpreted to be a shell hash layer where there was an increase in the amount of calcium (Figure 5.3).

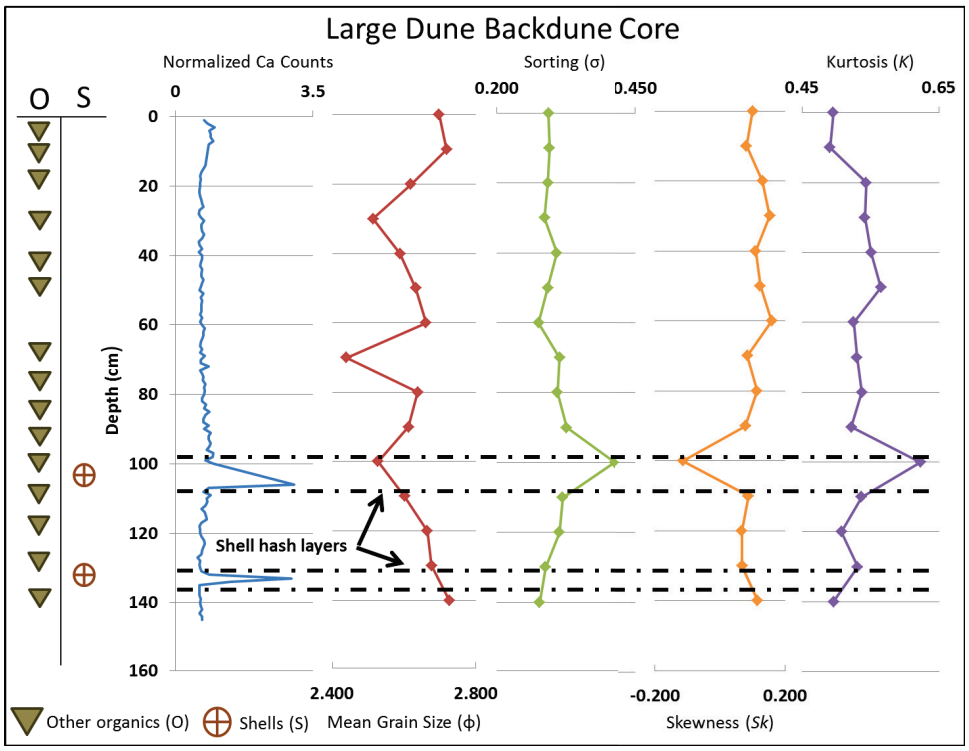

Fig. 5.3. Core results for back dune (Core D) of Site 3. There is an increase in calcium counts at approximately 1.1 m and 1.3 m. Blue line is the amount of calcium, red line is the mean grain size, green line is the sorting, orange is the skewness and purple is the kurtosis [Weymer, 2014].

The presence of shells from Core D provides confidence that the GPR data is showing amplitudes from the change in material in the subsurface as opposed to water content. Figures 5.4 and 5.5 show that GPR reflection amplitudes correspond to variation in grain size from a shell hash layer. This conclusions was made because the core was taken in the upper meter of the dune which is further away from the water table. The amount of water would be minimal near the surface, and the GPR response is consistent with coring observations.

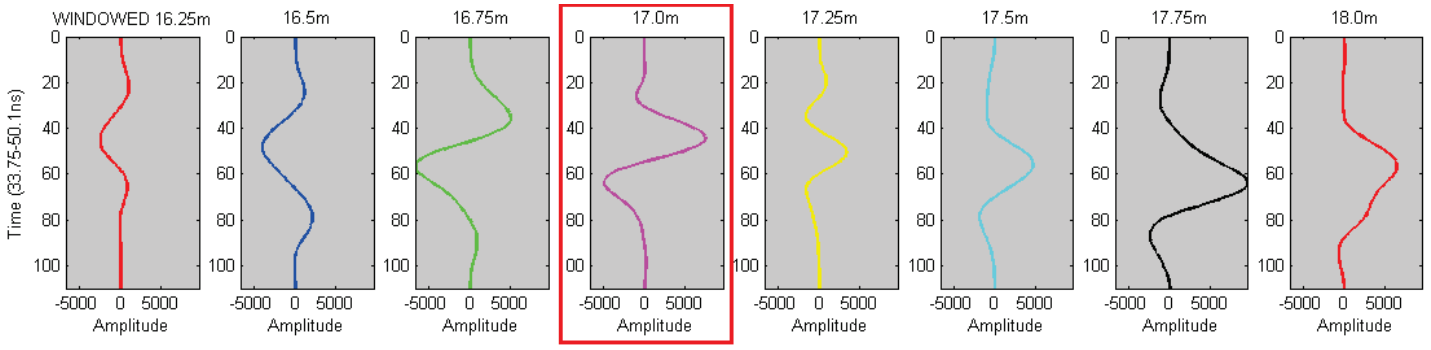

Fig. 5.4. Traces of GPR data from Site 3 bordering Core D. The core intersects at approximately 17 m. Reflection amplitudes are interpreted to occur from shell hash layer.

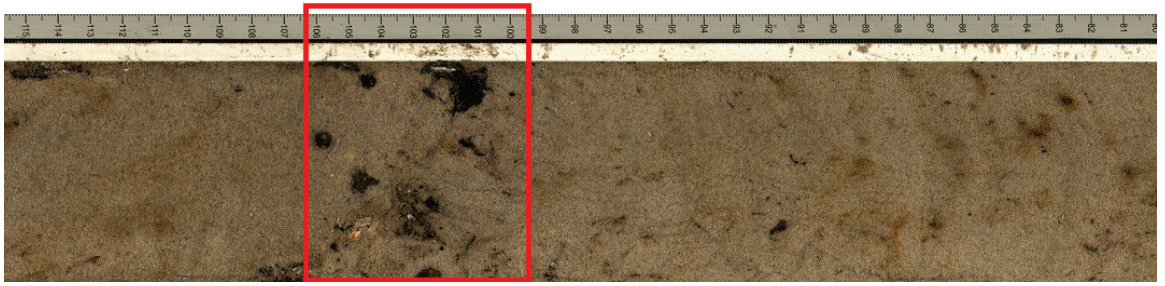

Fig. 5.5. Cropped image of high resolution scan of Core D around a depth of 100 cm of the core, which is approximately 1 meter above sea level. GPR traces at the same depth show amplitudes that correspond to the change in grain size. Modified from Weymer [2014]

6. SUMMARY

Instantaneous frequency plots reveal traces that exhibit anomalous features. In the three field cases, the anomalous feature is a phase response with a near-zero slope in the high-frequency region. To emphasize this response, an instantaneous frequency was calculated by taking the inverse of the slope. As the slope approaches zero, the instantaneous frequency attribute grows unbounded. In the field examples including merging beds, the slope of the phase response approached zero resulting in an instantaneous frequency spike. This result was consistent except for the last example where the beds did not merge. There was not an instantaneous frequency spike, and therefore no anomalous phase response. Figure 6.1 compares the instantaneous frequency for two field examples where the beds merged, a field example where the beds were parallel, and the Ricker model. This clearly shows that there is a useful attribute associated with merging beds in the form of a spike in instantaneous frequency. Two field examples show anomalous instantaneous frequency where merging beds were observed whereas no distinct spikes in instantaneous frequency were observed for both the Ricker model and the field example where beds were not merging.

The Ricker model does not show an anomalous attribute where the beds merge. Though this does not agree with the field results, it simply suggests that the Ricker model is not an accurate model for GPR reflections. This model is frequently used for synthetic seismic reflection data however it does not conform to observations with GPR data. It is possible that a differently shaped Ricker wavelet, such as the 90° wavelet, could be a more accurate representation of GPR wavelets.

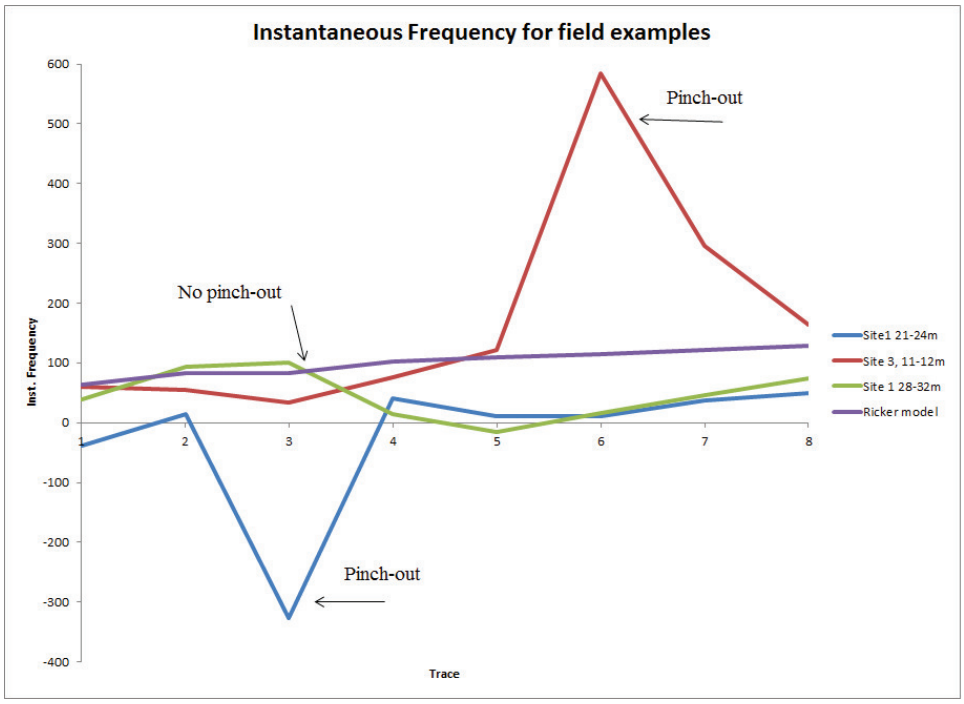

Fig. 6.1. Instantaneous frequency of all examples.

The phase response, in all cases, presented noise at the low frequency region. This is attributed to the low-pass filter removing only high frequency components of the signal. Had a high-pass filter been used, the low frequency content would have been removed and the noise would be located in the high frequency region. However, a high-pass filter would not be appropriate for this sort of data. It would remove the low frequencies, and depending on the aggressiveness of the filter, would likely take out any anomalous response associated with the beds merging.

The algorithm presented here shows consistent attribute trends; however it is a very subjective and sensitive process. The initial traces were picked and cropped such that the Hann windowing was able to fairly represent the data while windowing the edges of the trace. The low-pass filter has a significant effect on the data so it is important to apply a light hand in order to preserve the authenticity of the

data. Further research would allow a more accurate and automated system to ensure consistency in the spectral analysis process.

6.1 Research Impact

Attribute analysis is not used frequency for GPR; however it is extremely useful for environmental applications. Orlando [2002] analyzed how attributes from spectral analysis was successful for detecting contaminants using GPR. The application of spectral analysis may be applied for a variety of cases including archaeological investigation, fracturing, and geotechnical problems. This analysis is useful because it emphasizes locations of merging reflectors whether at a single interface or at locations where two beds "add" together. Being able to detect to a finer degree the location of a fault or fracturing would constitute a significant advancement in GPR resolution.

Direct application of the spectral analysis could influence sedimentological interpretations of internal dune structure from Padre Island. The results from Site 1 reveal approximate locations where internal dune structure comes in contact with the storm surface. This can then be used to calculate the depth of the storm surface. With other information, like sand accumulation rates and erosional patterns, it could be possible to date a storm event.

6.2 Further Research

The Ricker model presented in this research was not an accurate representation of GPR reflectivity. A further research recommendation is to construct an improved reflectivity model that agrees with GPR data. It is hypothesized that the spectral analysis shown here might would be consistent with research done for seismic applications; however, it is not clear why this model is not accurate for GPR. This discrepancy needs to be explored further.

The motivation of the project was to derive an analysis to detect buried sand sheets associated with tsunamis. The spectral analysis is a step in the right direction towards accomplishing that task. There was some field data collected at Padre Island over an area that appeared to be a washover. This is where a hurricane storm pushes over the front dunes, and spreads outwards in a fan-like shape. Figure 6.2 is a roughly processed GPR profile over the washover site. These data could help analysis of thinning sand sheets from storm events like that of a tsunami.

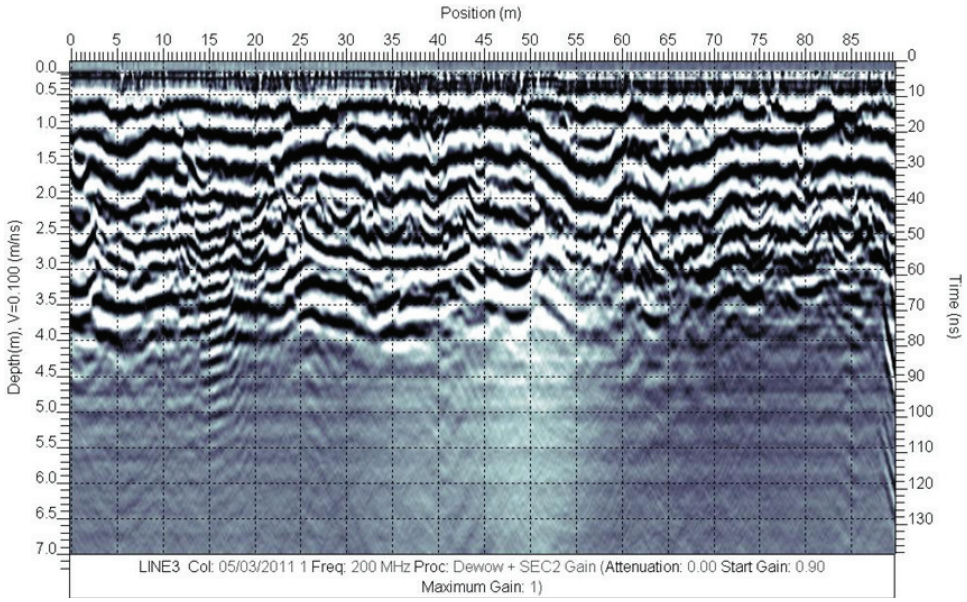

Fig. 6.2. Processed GPR profile from North Padre Island over a hypothesized washover.

Applying a spectral analysis to large amounts of data could have profound results. The amount of data used for this analysis is minimal compared to the scale of a GPR survey. The next step of performing a spectral analysis is develop have an automated system that sweeps through a large dataset. At points of merging beds or where contacts occur, the instantaneous frequency would [resumably show anomalous spikes. When plotted, these would appear as "bright spots" in the data. When

analyzing subsurface layers or targets, these “bright spots” would allow the user to rapidly interpret structure to a much finer degree.

Amplitude Versus Offset is a successful technique used in seismic reflection studies. The technique has also had success in GPR although it is not as heavily tested and studied. Future research recommendations would be to do the same analysis for Common Mid-Point data collected at Padre Island. This would allow more insight into showing that spectral analysis can be used for both data collection arrays and in sedimentary systems.

Lastly, another interest of further research is to apply the same technique to other GPR data from an archaeological site or for groundwater detection using varying frequency antennas. Researchers have used frequencies in the range 100-400 MHz for spectral analysis; however GPR is capable of using higher frequencies. It would be interesting to see if the antenna frequency has a large impact on the attribute analysis. Limited research has shown that the technique is successful, however more analysis should be performed to test a variety of applications.

REFERENCES

Annan, A., 1999, Practical processing of GPR data: Sensors and Software Inc. Mississauga Canada, 1–16.

Annan, A., and D. Butler, 2005, Ground-penetrating radar from near-surface geophysics: Society of Exploration Geophysicists.

Annan, A., and H. Jol, 2009, Electromagnetic principles of ground penetrating radar from ground penetrating radar theory and applications: Elsevier.

Bailey, S., and C. Bristow, 2000, The structure of coastal dunes: observations from ground penetrating radar (GPR) surveys: Proc. SPIE, **4804**, 660.

Baker, G., 1998, Applying AVO analysis to GPR data: Geophysical Research Letters, **25**, 397–400.

Barnes, A., 2007, A tutorial on complex seismic trace analysis: Geophysics, **72**, W33–W43.

Berthling, I., B. Etzelmuller, K. Isaksen, and J. Sollid, 2001, Rock glaciers on Prins Karls Forland. II: GPR sounding and the development of internal structures: Permafrost and Periglacial Processes, **11**, 257–369.

Bradford, J., 1999, Characterizing shallow aquifers with wave-propagation based geophysical methods: imaging and attribute analysis: PhD Dissertation, Rice University.

Bradford, J., and J. Deeds, 2006, Ground-penetrating radar theory and application of thin-bed offset-dependent reflectivity: Geophysics, **71**, K47–K57.

Bristow, C., P. Chroston, and S. Bailey, 2000, The structure and development of foredunes on a locally prograding coast: insights from ground-penetrating radar surveys, Norfolk, UK: Sedimentology, **47**, 923–944.

Cassidy, N., and H. Jol, 2009, Ground penetrating radar data processing, modelling and analysis from ground penetrating radar theory and applications: Elsevier.

Castagna, J., and M. Backus, 1993, Offset-dependent reflectivity - theory and practice of AVO analysis: Society of Exploration Geophysicists.

Castanga, J., 1993, Petrophysical imaging using AVO: The Leading Edge, 172–178.

Davis, J. L., and A. Annan, 1989, Ground-penetrating radar for high-resolution mapping of soil and rock stratigraphy: Geophysical Prospecting, **37**, 531–551.

Deparis, J., and S. Garambois, 2009, On the use of dispersive APVO GPR curves for thin bed properties estimation: Theory and application to fracture characterization: Geophysics, **74**, J1–J12.

Engheta, N., and C. H. Papas, 1982, Radiation patterns of interfacial dipole antennas: Radio Science, **17**, 1557–1566.

Everett, M., 2013, Near surface applied geophysics: Cambridge University Press. (to appear).

Fukui, K., T. Sone, J. Sterlin, C. Torielli, and J. Mori, 2007, Ground penetrating radar sounding on an active rock glacier on James Ross Island, Antarctic Peninsula region: Polish Polar Research, **28**, 13–22.

Gracia, V., J. Canas, L. Pujades, J. Clapes, O. Caselles, F. Garcia, and P. Osorio, 2000, GPR survey to confirm the location of ancient structures under the Valencian Cathedral (Spain): Journal of Applied Geophysics, **43**, 167–174.

Griffiths, D., 1989, Introduction to electrodynamics: Prentice Hall. (Third Edition).

Ikelle, L., and L. Amundsen, 2005, Introduction to petroleum seismology: Society of Exploration Geophysicists.

Jackson, J., 1999, Classical electrodynamics: Wiley& Sons Inc. (Third Edition).

Jenkins, F., and H. White, 1957, Fundamentals of optics: McGraw Hill Book Company.

Kallweit, R., and L. Wood, 1982, The limits of resolution of zero-phase wavelets: Geophysics, **47**, 1035–1046.

Knapp, R., 1990, Vertical resolution of thick beds, thin beds, and thin-bed cyclothems: Geophysics, **55**, 1183–1190.

Knight, R., 2001, Ground penetrating radar for environmental applications: Earth and Planetary Science, **29**, 229–255.

Lutz, P., S. Garambois, and H. Perroud, 2003, Influence of antenna configurations for GPr survey: information from polarization and amplitude versus offset measurements: Geological Society London, **211**, 299–313.

Nabighian, M., 1987, Electromagnetic methods in applied geophysics: Society of Exploration Geophysics.

Neal, A., 2004, Ground-penetrating radar and its uses in sedimentology: principles, problems and progress: Earth-Science Reviews, **66**, 261–330.

Olhoeft, G., 1998, Electrical, magnetic, and geometric properties that determine ground penetrating radar performance: Seventh International Conference on Ground Penetrating Radar. University of Kansas Lawrence KS, 177–182.

Oppenheim, A., and R. Schafer, 2010, Discrete-time signal processing: Prentice Hall. (Third edition).

Orlando, L., 2002, Detection and analysis of LNAPL using the instantaneous amplitude and frequency of ground-penetrating radar data: Geophysical Prospecting, **50**, 27–41.

Reynolds, J., 1997, An introduction to applied and environmental geophysics: John Wiley & Sons Ltd.

Ricker, N., 1953, Wavelet contraction, wavelet expansion and the control of seismic resolution: Geophysics, **18**, 769–792.

Schmalz, B., and B. Lennartz, 2002, Analysis of soil water content variations and GPR attribute distributions: Journal of Hydrology, **267**, no. 3-4, 217–226.

Streich, R., and J. van der Kruk, 2007, Accurate imaging of multicomponent GPR data based on exact radiation patterns: IEEE Transcations on Geoscience and Remote Sensing, **45**, 93–103.

Taner, M., F. Koehler, and R. Sheriff, 1979, Complex seismic trace analysis: Geophysics, **44**, 1041–1063.

Weise, B., and W. White, 1980, Padre Island National Seashore: A guide to the geology, natural environments, and history of a Texas barrier island: University of Texas Bureau of Economic Geology. (Guidebook 17).

Weymer, B., 2014, A geologic characterization of the alongshore variability in beach-dune morphology: Padre Island National Seashore, Texas: Master's thesis, Texas A&M University. (to appear).

White, W., 1978, Land and water resources, historical changes, and dune criticality: Mustang and North Padre Islands, Texas: University of Texas Bureau of Economic Geology.

Widess, M., 1973, How thin is a thin bed?: Geophysics, **38**, 1176–1180.

Zeng, H., 2009, How thin is a thin bed? an alternative perspective: The Leading Edge, 1192–1197.

———, 2010, Geologic significance of anomalous instantaneous frequency: Geophysics, **75**, P23–P30.

APPENDIX 1

MATLAB EXAMPLE CODE

```
data = xlsread('ricker.xls'); %data input
datasize = size(data);
plength = 1/2*(datasize(1));
wind = hann(datasize, 'periodic'); %windowing the data
datawind=wind.*data;
f=0.1;
[b,a]=butter(4,f,'low'); %apply low-pass filter
filt=filtfilt(b,a,datawind);
for i=1:datasize(2)
    vectorme = filt(:,i); %splitting matrix into vectors
    y(:,i) = fft(vectorme); %FFT of each vector
    for j=1:datasize(1)
        y_real(j,i) = real(y(j,i));
        y_imag(j,i) = imag(y(j,i));
        y_phase(j,i) = atan(y_imag(j,i)/y_real(j,i)); %phase of ...
            each vector
        y_amp(j,i) = sqrt(y_real(j,i)^2+y_imag(j,i)^2); ...
            %instantaneous amplitude of each vector
    end
end
```

VITA

Name:	Renee Rose Francese
E-mail Address:	rrfrancese@tamu.edu
Address:	Renee Francese c/o Department of Geology and Geophysics MS 3115 Texas A&M University College Station, TX 77843
Education:	B.S., Geophysical Engineering, Colorado School of Mines, 2010 M.S., Geophysics, Texas A&M University, 2012